Polymer Journal (2023) 55:297–316
https://doi.org/10.1038/s41428-022-00727-8

REVIEW

Indoor photovoltaic energy harvesting based on semiconducting π-conjugated polymers and oligomeric materials toward future IoT applications

Sunbin Hwang[1] · Takuma Yasuda[1,2]

Received: 19 September 2022 / Revised: 5 October 2022 / Accepted: 5 October 2022 / Published online: 15 November 2022

Abstract

With the advancement of artificial intelligence computing systems that can collect, analyze, and utilize metadata from our activities and surrounding environments, establishing self-powered electronic systems/networks supported by energy harvesters is strongly desired. With the lowering of power consumption in contemporary IoT electronics such as wireless sensors, indoor organic photovoltaic devices (iOPVs), which can be driven under ambient indoor light, have recently attracted significant interest as self-sustainable eco-friendly power sources. iOPVs based on organic semiconductors have unique advantages, such as light weight, flexibility, solution processability, and feasibility of low-temperature mass production. Additionally, the spectral tunability and high optical absorptivity of organic semiconductors make iOPVs more effective as energy harvesters in indoor lighting environments. With recent intensive research effort, iOPVs have realized the delivery of high power conversion efficiencies exceeding 25% with output power densities of several tens to a hundred μW cm^{-2}, which are sufficient to drive various low-power electronics compatible with the IoT. This review article focuses on recent progress in iOPVs based on π-conjugated polymers and oligomeric materials and outlines their fundamental principles and characterization techniques.

Introduction

Electronic devices have become indispensable tools for modern life and society. With the emergence of novel low-power electronics such as wireless sensors and portable/wearable devices [1–3], the Internet of Things (IoT) is rapidly developing and spreading. In this circumstance, combined with artificial intelligence (AI) computing systems that enable metadata analysis, the exponential growth of off-grid smart sensor networks for collecting big data is desirable. In the next decade, it is expected that billions to trillions of wireless sensors will be installed to support our lives, industry, commerce, logistics, and infrastructure. Currently, most IoT devices are powered by batteries, which require periodic replacement and maintenance owing to their relatively short lifespans as power sources. Considering advanced next-generation IoT ecosystems, powering a huge number of IoT devices solely from batteries would not be practically sustainable from environmental, resource, safety, and cost perspectives [4]. Energy harvesting technologies that collect unused energy from sources such as ambient light (photovoltaic harvesting) [5–7], heat (thermoelectric harvesting) [8, 9], and mechanical vibration/movement (piezoelectric and triboelectric harvesting) [10] have recently attracted significant interest as key elements for solving these problems and constructing self-sustainable IoT ecosystems.

Photovoltaic devices (PVs) are widely used as solar cells in outdoor applications [11]. PVs are also capable of generating power (even though relatively low power) by harvesting artificial indoor light. Although sunlight is not available in all locations and at all times, ambient indoor lighting is always available to supply energy for operating low-power IoT devices. Unlike robust inorganic silicon-based PVs, organic PVs (OPVs) based on organic semiconductors have various inherent advantages such as light

✉ Sunbin Hwang
hwang@ifrc.kyushu-u.ac.jp

✉ Takuma Yasuda
yasuda@ifrc.kyushu-u.ac.jp

[1] Institute for Advanced Study, Kyushu University, Fukuoka, Japan

[2] Department of Applied Chemistry, Graduate School of Engineering, Kyushu University, Fukuoka, Japan

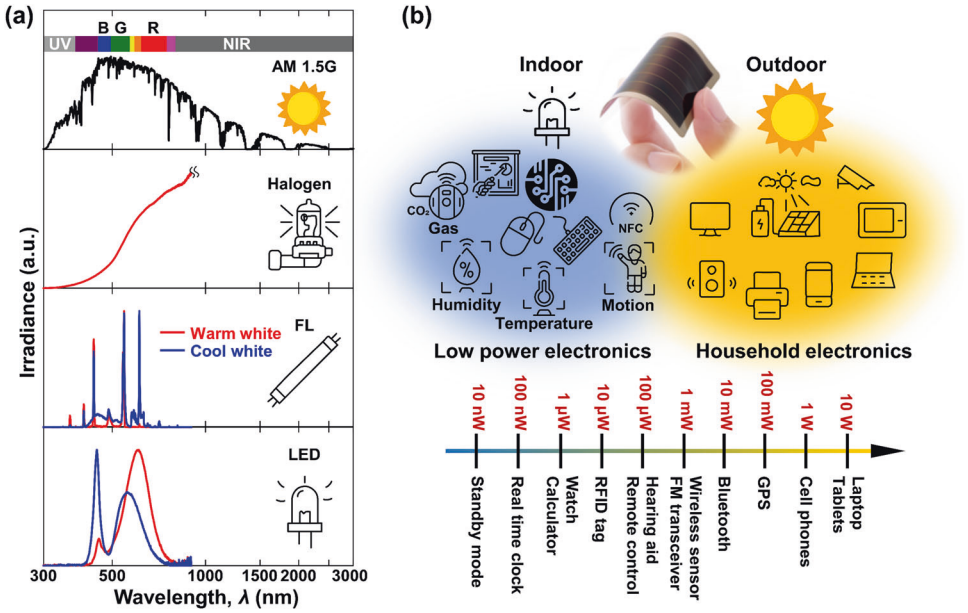

Fig. 1 **a** Comparison of emission spectra for various light sources: sunlight (AM 1.5 G), halogen lamp, fluorescent lamp (FL) and light-emitting diode (LED). **b** Power consumption by various IoT electronic devices and related energy harvesting capabilities of iOPVs [35]

weight, flexibility, solution processability, and cost-effective large-area manufacturing capabilities [12–16]. Moreover, OPVs can convert weak indoor light into electricity more efficiently than silicon-based PVs because of their spectral tunability and higher optical absorptivity, as well as the lower leakage currents of organic semiconductors. These features endow OPVs with great potential for application in versatile distributed power sources that can be implemented anywhere with any shape and size compatible with the IoT. The power conversion efficiencies (PCEs) of OPVs as solar cells have recently reached over 18% (for single-junction cells) under 1-sun conditions (AM 1.5 G, 100 mW cm^{-2}) [11, 17, 18]. However, it should be noted that high-performance OPVs under outdoor 1-sun conditions do not necessarily deliver high performance under dim-light indoor conditions. In other words, developing indoor OPVs (iOPVs) requires design guidelines different from those of conventional solar cells from the perspective of both materials chemistry and device physics [19–27].

The critical differences between indoor and outdoor PV systems are the emission spectra and power densities of the light sources available to them. In contrast to outdoor sunlight, for which the spectrum is widely distributed from the ultraviolet (UV) to the infrared (IR) region over the range of 280–3000 nm, the emission spectra of indoor lighting, as represented by fluorescent lamps (FLs) and white light-emitting diodes (LEDs), are typically limited to the visible range of 400–750 nm (Fig. 1a). Therefore, to achieve superior energy harvesting functionality, organic semiconductors with optical responses (absorptions) well matched spectrally with indoor light sources should be more favorable for iOPVs than the broad photoabsorption spectra preferred for outdoor solar cells. Moreover, the incident power densities of these indoor light sources (typically 0.1–1 mW cm^{-2}) are approximately two to three orders of magnitude lower than that of sunlight (AM 1.5 G, 100 mW cm^{-2}), so that the charge carrier densities are significantly reduced in iOPVs. In this case, Shockley–Read–Hall (SRH) recombination (also called trap-assisted recombination) via carrier trapping can be pronounced, which causes significant voltage loss. Over the past decade, several studies have been conducted to enhance the performance of iOPVs by considering these design guidelines. To date, PCEs of state-of-the-art iOPVs exceed 25% under white LED illumination [28, 29], delivering high output power densities of up to 110 μW cm^{-2} (at 1200 lx), which are sufficiently high to drive certain low-power electronic devices (Fig. 1b).

In this review, we introduce the basic principles of iOPVs and discuss their characterization methods along with key strategies for achieving superior indoor photovoltaic performance. Subsequently, we outline recent advances in iOPVs from the perspectives of materials chemistry and device engineering.

Basic principles and characterizations for iOPVs

Equivalent circuits and photovoltaic parameters

The performance of an iOPV is generally evaluated by PCE, that is, PCE (%) = $P_{out}/P_{in} \times 100$, where P_{out} (mW cm^{-2}) is the output power density of the device and P_{in}

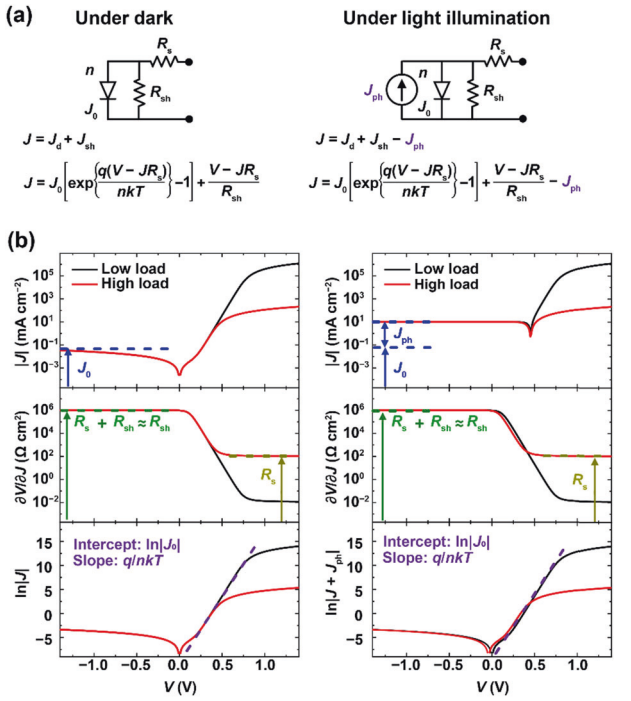

Fig. 2 **a** Equivalent circuits for iOPVs under dark (left) and light illumination (right) conditions. **b** Relationship between key parameters (R_s, R_{sh}, n, J_0, and J_{ph}) and J–V curves of iOPVs with a different load (R_s) measured under dark (left) and light illumination (right) conditions. J_d = current density flowing through the diode, J_{sh} = current density flowing through the shunt resistance, J_{ph} = photocurrent density generated from photodiode, J_0 = reverse saturation current density, n = ideality factor, k = Boltzmann constant, q = elementary charge, T = absolute temperature, R_s = series resistance, R_{sh} = shunt resistance

(mW cm^{-2}) is the incident light intensity (irradiance). P_{out} can be expressed as $P_{out} = V_{oc} \times J_{sc} \times FF$, where V_{oc} (V) is the open-circuit voltage, J_{sc} (mA cm^{-2}) is the short-circuit current density, and FF (%) is the fill factor. These parameters are extracted from the current density–voltage (J–V) curves measured under different P_{in} conditions. As schematically shown in Fig. 2a, the equivalent circuit model for iOPVs consists of a parallel-connected current source, diode, shunt resistance (R_{sh}), and an additional series resistance (R_s). While R_s is mainly attributed to the resistance of the bulk active layer and the interfacial contact resistance between the active layer and electrodes, R_{sh} originates from the leakage currents in the cell. Under dark conditions, the J–V characteristics of iOPVs represent the exponential response of a diode with a high J in the forward bias and low J in the reverse bias. Light illumination on iOPVs generates a photocurrent (J_{ph}); therefore, their J–V curves upon illumination are ideally the superposition of the dark and photocurrent characteristics (Fig. 2b). Accordingly, the J–V characteristics of an ideal device can be expressed using the Shockley diode equation, as follows (Eq. 1) [30–34]:

$$J = J_0\left[\exp\left\{\frac{q(V - JR_s)}{nkT}\right\} - 1\right] + \frac{V - JR_s}{R_{sh}} - J_{ph} \quad (1)$$

where J_0 is the reverse saturation current density, q is the elementary charge, n is the ideality factor of the diode, k is the Boltzmann constant, and T is the absolute temperature. When $n = 1$ (i.e., an ideal diode), carrier recombination in the depletion region is zero (or negligible), and the diffusion current is dominant. In contrast, when $n = 2$, carrier recombination dominates the dark current.

By solving Eq. 1 under short-circuit ($V = 0$) and open-circuit ($J = 0$) conditions, J_{sc} and V_{oc} are given by Eqs. 2, 3, respectively. Assuming an ideal device, i.e., J_0 and R_s are sufficiently small and J_{sc} and R_{sh} are sufficiently high, J_{sc} and V_{oc} can be expressed by the simple formulas shown on the right-hand side of each equation.

$$J_{sc} = \frac{1}{1 + R_s/R_{sh}}\left[J_0\left\{\exp\left(-\frac{qJ_{sc}R_s}{nkT}\right) - 1\right\} - J_{ph}\right] \cong -\frac{1}{1 + R_s/R_{sh}}J_{ph} \quad (2)$$

$$V_{oc} = \frac{nkT}{q}\ln\left\{1 + \frac{J_{ph}}{J_0}\left(1 - \frac{V_{oc}}{J_{ph}R_{sh}}\right)\right\} \cong \frac{nkT}{q}\ln\left(1 + \frac{J_{ph}}{J_0}\right) \cong \frac{nkT}{q}\ln\left(\frac{J_{ph}}{J_0}\right) \quad (3)$$

Based on Eq. 1, the key parameters R_s, R_{sh}, n, J_0, and J_{ph} can be extracted from the measured J–V curves (Fig. 2). R_s and R_{sh} are readily determined from the inverse slopes ($\partial V/\partial J$) of the forward and reverse J–V curves, respectively, whereas n and J_0 can be roughly estimated from the slope and intercept, respectively, of the linear portion of the dark ln(|J|)–V curve in the forward bias. Finally, J_{ph} can be deduced using the extracted parameters (R_s, R_{sh}, n, and J_0), according to Eq. 2. The accuracy of J–V curve fitting and analysis can be verified from the integrity of the J_{ph} and J_{sc} values. For actual iOPVs, the incident light intensity (irradiance) has a significant effect on these parameters. Unlike the situation for sunlight, iOPVs exhibit peculiar behavior, especially under dim-light illumination (low P_{in}) conditions; therefore, an accurate and detailed analysis is needed, as is discussed later.

V_{oc} attenuation under dim-light indoor conditions is a critical issue that causes PCE reductions in iOPVs [29, 35]. According to Eq. 3, V_{oc} can be maintained high by sufficiently reducing J_0 and increasing R_{sh}. However, under dim-light conditions, the resulting photocurrent (J_{ph}) is inevitably small because of the low carrier density. In this case, the

contributions of the dark and leakage currents (J_0 and J_{sh}) become non-negligible and cause significant V_{oc} attenuation. Figure 3 shows the typical V_{oc}–J_{ph} relationships simulated for iOPVs with different J_0 values. A steep reduction in V_{oc} with decreasing J_{ph} is universally observed for all J_0 conditions (10^{-7}–10^{1} mA cm^{-2}). In the high-J_{ph} regime satisfying $V_{oc} \ll J_{ph}R_{sh}$, V_{oc} exhibits a quasi-linear dependence on ln(J_{ph}) and satisfies the relationship $V_{oc} = (nkT/q)\ln(J_{ph}/J_0)$, as in the case of conventional solar cells. However, in the low-J_{ph} regime with $V_{oc} \gg J_{ph}R_{sh}$, the degree of V_{oc} attenuation becomes more pronounced and follows the relationship $V_{oc} = (nkT/q)\ln\{1 + (J_{ph}/J_0)(1 - (V_{oc}/J_{ph}R_{sh})\}$. The inflection points of the V_{oc} attenuation curves are found to be susceptible to J_0, suggesting that a device with a lower J_0 can maintain a higher V_{oc}, even under dimly lit conditions. Thus, modulating these parameters can effectively suppress V_{oc} attenuation under indoor conditions, leading to high PCEs over a wide illuminance range for iOPVs. It can be concluded that a higher V_{oc} under AM 1.5 G and a smaller voltage loss under indoor conditions are crucial for iOPVs.

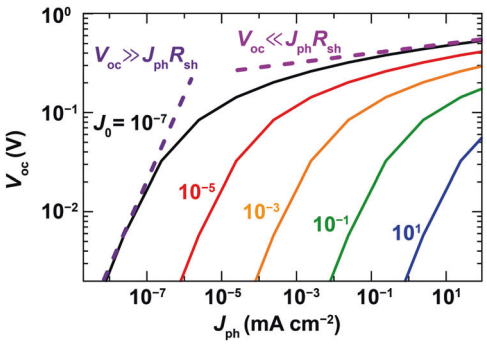

Fig. 3 Simulated V_{oc}–J_{ph} relationships of ideal iOPVs ($n = 1$) with different J_0 in the range of 10^{-7}–10^{1} mA cm^{-2}

The parasitic resistances (R_s and R_{sh}) also have a large impact on the resulting FFs of iOPVs [36–38]. It is evident that the largest possible R_{sh} (ideally ∞) and the smallest possible R_s (ideally 0) are preferred to enhance the FF and thereby maximize P_{out}. Figure 4 shows the simulated J–V characteristics of iOPVs with different R_s and R_{sh} (R_s/R_{sh} ratios). Under indoor conditions, R_s and R_{sh} show effects that are quite different from those found under outdoor conditions. Evidently, under high illuminance ($P_{in} = 100$ mW cm^{-2}, Fig. 4a), the photovoltaic characteristics are mainly governed by R_s, and the impact of R_{sh} is very limited. In contrast, under low illuminance ($P_{in} =$ 1 mW cm^{-2}, Fig. 4b), R_{sh} becomes more crucial for indoor photovoltaic performance, and R_s no longer has a substantial impact on the overall J–V characteristics. This is because the trap-assisted recombination associated with R_{sh} becomes dominant in the carrier recombination processes at low carrier densities. Therefore, increasing R_{sh} by suppressing trap-assisted recombination is vital for achieving high FFs and thereby high PCEs for iOPVs. These basic design principles are quite different from the guidelines established for conventional solar cells.

Evaluation of iOPV efficiency

The PCEs of iOPVs are strongly dependent on the type of indoor light source (i.e., emission spectra and illuminance). To determine their PCEs accurately, we need to select a suitable light source and evaluate its power density (P_{in}). The 1-sun condition ($P_{in} = 100$ mW cm^{-2}) with a simulated AM 1.5 G spectrum (Fig. 1a) is the global standard used for characterizing outdoor PVs. However, neither indoor light sources nor a standard protocol have been specified for evaluating iOPVs. This is because, unlike the sun, we use a variety of light sources, including LEDs and FLs, in indoor environments. As shown in Fig. 1a, there are significant differences in the

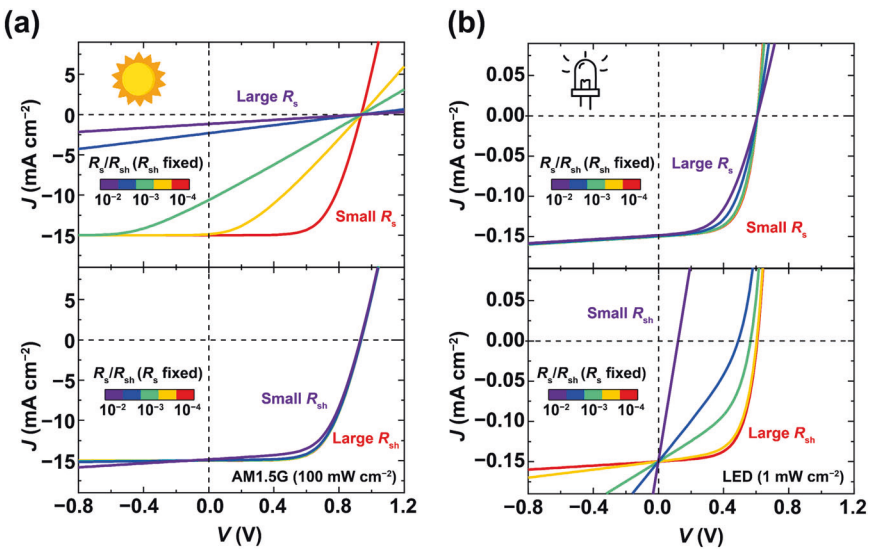

Fig. 4 Comparison of J–V characteristics depending on R_s and R_{sh} under (**a**) outdoor and (**b**) indoor conditions

emission spectra of artificial indoor light sources. Accordingly, establishing and standardizing appropriate evaluation methodologies for iOPVs are current challenges [39, 40].

In general, indoor light is measured as photometric illuminance L (lx), which is typically in the range of 100–1000 lx. Theoretically, L and P_{in} of an arbitrary light source can be calculated by integrating the spectral irradiance $F(\lambda)$ (mW cm^{-2} nm^{-1}) using Eqs. 4 and 5:

$$P_{in} = \int F(\lambda)\mathrm{d}\lambda \tag{4}$$

$$L = K_m \int F(\lambda)V(\lambda)\mathrm{d}\lambda \tag{5}$$

where K_m is a constant representing the maximum luminous efficiency ($K_m = 683$ lm W^{-1}) and $V(\lambda)$ denotes the spectral luminous efficiency function for human photopic vision. In practice, L can be measured using an illuminance spectrophotometer. Figure 5a depicts the typical irradiance–illuminance (P_{in}–L) relationships of various indoor light sources. It should be noted that different light sources afford different P_{in} values, even at the same L, because of the different matching levels between the light-source emission spectra and human eye photopic sensitivity. Under a low L of 200 lx with warm-white LED illumination (3000 K), which corresponds to living environments, P_{in} is ~60 μW cm^{-2}, whereas P_{in} increases to ~300 μW cm^{-2} under a high L of 1000 lx. However, these incident P_{in} values are less than 0.1% and 1%, respectively, of outdoor 1-sun illumination. Note also that, even if L is the same, if the light-source color temperature is different, P_{in} differs substantially. Therefore, to evaluate iOPV efficiency, not only the illuminance of the incident light but also its spectral irradiance (or P_{in}) and color temperature should be clarified as a prerequisite. According to recent research, it is recommended that iOPV efficiencies should be evaluated by using a white LED as standard indoor lighting by specifying its color temperature and spectral irradiance.

What is the limit of the iOPV efficiency? The maximum PCEs of iOPVs can be assessed based on the Shockley–Queisser (SQ) limits [41] for various light sources, with the assumption that photon energies above the bandgap (E_g) of the material are all absorbed and charge carriers are fully extracted. Theoretical simulations reveal that the optimal E_g of iOPVs for white LED illumination is 1.7–1.9 eV (*ca.* 650–730 nm) [39, 40, 42, 43]. As shown in Fig. 5b, for AM 1.5 G illumination, it is well known that the SQ-limited PCE is ~33%, as the photovoltaic materials have an E_g of 1.1–1.3 eV. According to the best research-cell efficiencies chart provided by the National Renewable Energy Laboratory (NREL) [11], crystalline silicon (c-Si) solar cells with E_g of ~1.1 eV have achieved significantly high PCEs of up to 27.6%, which approach the SQ limit for 1-sun illumination. However, unlike these outdoor conditions, photovoltaic materials with a much

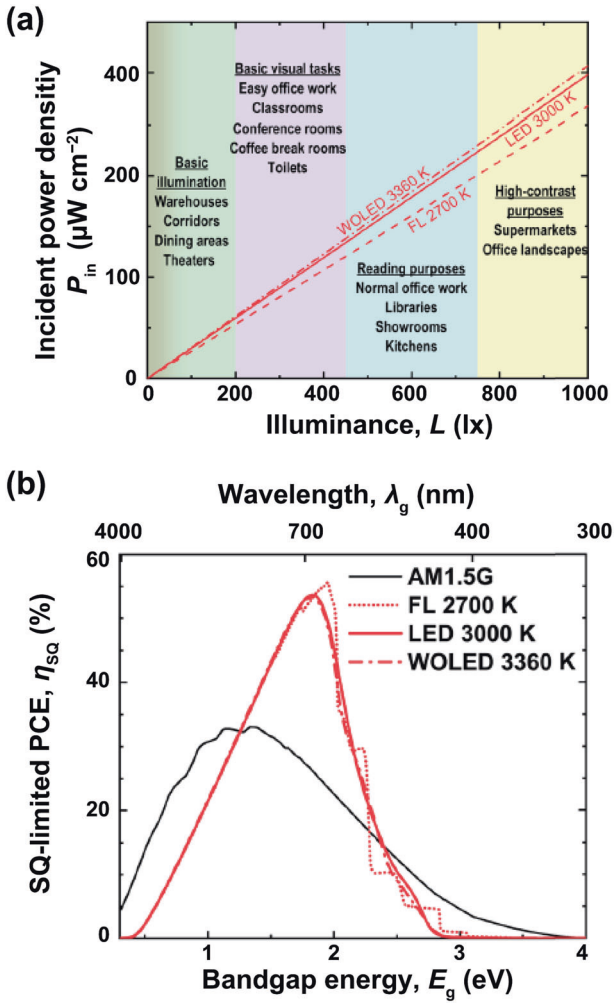

Fig. 5 **a** Incident power densities (P_{in}) of selected indoor light sources as a function of illuminance (L). **b** Shockley–Queisser (SQ)-limited power conversion efficiency (PCE) *vs.* bandgap energy (E_g) relationships depending on incident light sources ($L = 300$ lx for all artificial indoor light sources, except for AM 1.5 G). Reproduced from reference [40] with permission from Royal Society of Chemistry

wider E_g are more suitable for indoor conditions, leading to ideal SQ-limited PCEs as high as ~57%. This is primarily because the emission spectra of indoor light sources are relatively narrow compared to sunlight, so the irradiated photons can be more effectively utilized by organic semiconductors while suppressing thermalization and transparency losses. The best PCEs of iOPVs reported thus far are ~30% under illumination with a warm-white LED (3000 K) [29]. There is still room for improvement in terms of both the materials and devices for future IoT applications.

Recent advances in iOPVs

To achieve high-efficiency iOPVs, the design of appropriate organic semiconductor materials that play the core role in

the active layer is of primary importance. Although iOPVs are a class of recently emerging energy-harvesting devices, we can take advantage of material technologies for organic solar cells that have been accumulated over the last two decades [12–18]. However, as described in Section "Basic principles and characterizations for iOPVs", the design guidelines for iOPVs differ from those for conventional solar cells in several respects. In particular, spectral matching with indoor light sources and suppression of V_{oc} reduction under low illuminance are key factors. For indoor applications, the optimal E_g for iOPV materials is comparatively large (1.7–1.9 eV), as only photons in the visible region need to be harvested.

The photoactive layers of iOPVs typically consist of electron donor and acceptor materials, which intermix with each other to form bulk heterojunction (BHJ) nanostructures. The BHJ layer with a typical thickness of ~0.1 μm performs all main functions (i.e., photoabsorption, charge separation, and charge transport) in iOPVs. Therefore, selection and composition of the donor and acceptor materials are critical to iOPV performance. As in the case of organic solar cells, the recent advent of non-fullerene acceptors (NFAs) [44–47] has greatly expanded the choice and combinations of donors and acceptors, even for iOPVs. In this section, we review the recent advances in iOPVs from a material perspective by categorizing them into the following four main groups: (i) polymer donor–fullerene acceptor binary systems [48–67], (ii) small-molecule (SM) donor–fullerene acceptor binary systems [35, 54, 57, 60, 68], (iii) polymer donor–NFA binary systems [28, 29, 62, 64, 66, 69–92], and iv) ternary and quaternary systems [55, 69–71, 76, 77, 81, 82, 93]. The chemical structures of the representative polymer/SM donors and fullerene/nonfullerene acceptors used for iOPVs are shown in Figs. 6, 7, respectively. Comprehensive iOPV data, categorized into fullerene-based and NFA-based BHJ systems, are presented in Tables 1, 2, respectively.

Polymer donor–fullerene acceptor binary systems

The initial iOPVs reported in the 2010s were based on polymer:fullerene BHJ systems, in which a classical semiconducting polymer, regioregular poly(3-hexylthiophene) (P3HT, Fig. 6), was used in combination with the soluble fullerene derivatives $PC_{61}BM$ and $PC_{71}BM$ (Fig. 7) [38, 49, 53]. However, their indoor photovoltaic performance was unattractive because of their low V_{oc} (<0.5 V) and low PCEs (<9%). To enhance the V_{oc} of iOPVs, an indene-C_{60} bisadduct (ICBA) with a shallower lowest unoccupied molecular orbital (LUMO) energy level ($E_{LUMO} = -3.74$ eV) was subsequently applied as an acceptor instead of $PC_{61}BM$ ($E_{LUMO} = -3.90$ eV) [53, 56, 58]. The larger energy offset between the highest occupied molecular orbital (HOMO) of P3HT and the LUMO of ICBA resulted in a V_{oc} higher than that of the P3HT:PCBM system. Consequently, the P3HT:ICBA-based iOPVs achieved an improved PCE of 13% with a higher V_{oc} of 0.73 V under LED illumination (500 lx).

The search for high-performance semiconducting polymers has continuously improved the performance of fullerene-based iOPVs. In 2015, Mori et al. reported the indoor photovoltaic properties of a PTB7-Th:$PC_{71}BM$ system [48]. Under LED illumination (890 lx), the PTB7-Th:$PC_{71}BM$-based iOPV exhibited a higher PCE (11.6%) than the c-Si cell (9.6%) because of its higher V_{oc} (0.62 V) than that of the c-Si cell (0.43 V). The higher V_{oc} and well-matched absorption spectrum are advantages of iOPVs over Si-based cells for indoor energy harvesting. Subsequent studies by other research groups further improved the PCEs of PTB7-Th:$PC_{71}BM$-based iOPVs to ~16% [53, 65].

In 2016, Lee et al. compared the indoor photovoltaic properties of P3HT, PTB7, and PCDTBT (Fig. 6) as polymer donors in combination with PCBM [49]. The PCDTBT:$PC_{71}BM$-based iOPV exhibited the best performance among them, affording a high PCE of 16.6% with a high V_{oc} of 0.72 V under FL illumination (300 lx). Although the PTB7:$PC_{71}BM$-based device showed better performance than the PCDTBT:$PC_{71}BM$-based device under AM 1.5 G, the indoor PCE tended to be lower (14.6%) because of its narrower E_g. Yin et al. subsequently reported comparably high indoor PCEs of up to 18.7% with the same PCDTBT:$PC_{71}BM$ system under a white LED (300 lx) [55, 57]. Inspired by the success of PCDTBT, since 2019, various benzothiadiazole-containing wide-bandgap donor polymers, such as PPDT2FBT [59, 64], PDTBTBz-2F [61], and P3TEA [66], have been tested in combination with PCBM for iOPVs, and they have exhibited high PCEs under LED or FL illumination (Table 1). In particular, the PDTBTBz-2F:$PC_{71}BM$-based iOPVs achieved a notably high PCE of 23.1% with V_{oc} of 0.82 V, generating P_{out} as high as ~65 μW cm^{-2} under LED illumination (1000 lx) [61], which is the best indoor photovoltaic performance among reported fullerene-based iOPVs. Importantly, the PDTBTBz-2F:$PC_{71}BM$-based device afforded a PCE as low as 6.9% under 1-sun conditions, suggesting that materials unsuitable for outdoor solar cells may be more suitable for indoor energy harvesting. It is also worth mentioning that a relatively thick photoactive layer can be more suitable for iOPVs [50, 57, 59, 66, 67]. For the PPDT2FBT:$PC_{71}BM$-based iOPVs, even devices with thick BHJ photoactive layers (390–870 nm) demonstrated excellent indoor photovoltaic performance with PCEs of 16.0–12.5% [59]. According to Eq. 2, J_{sc} is inversely

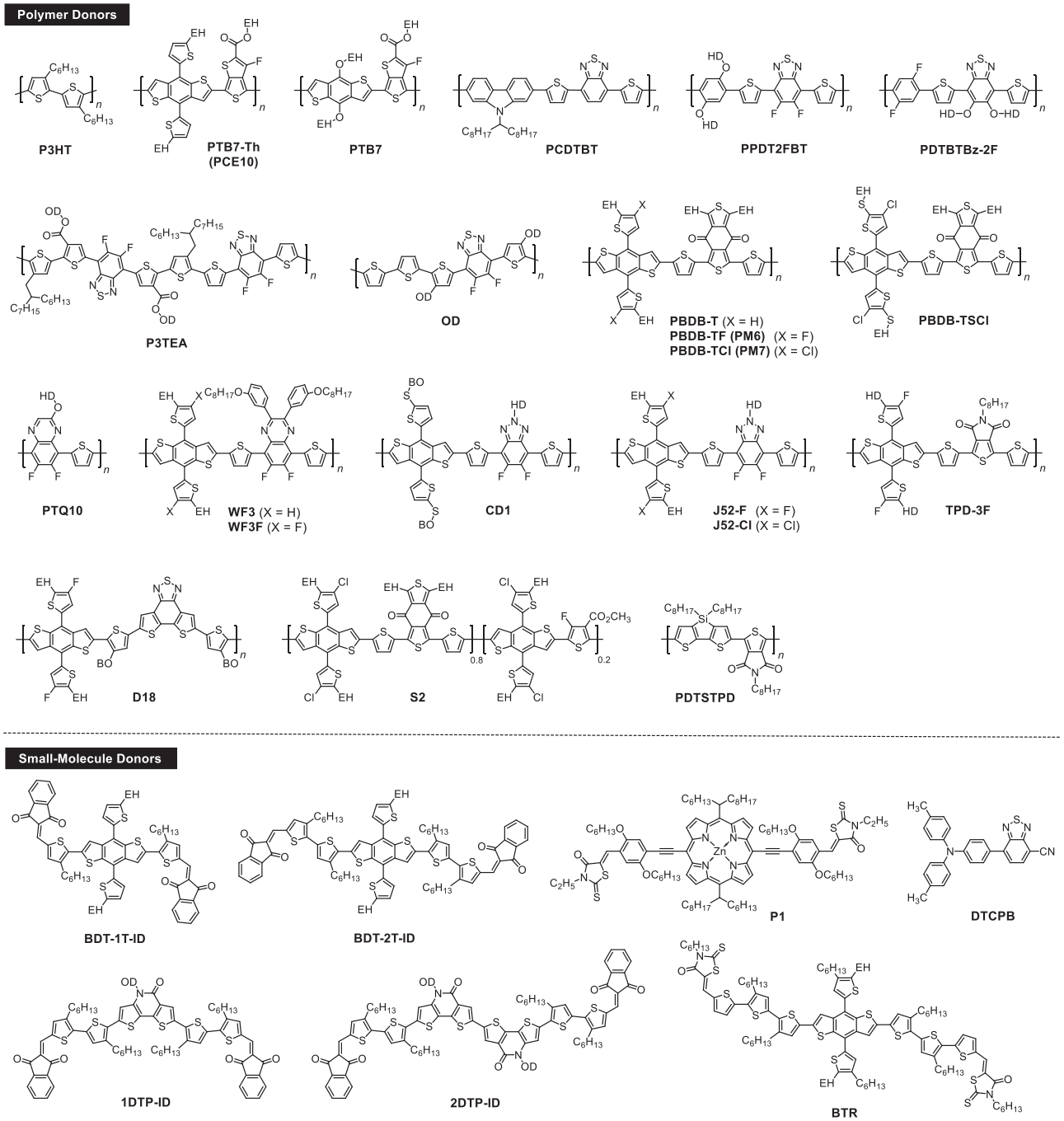

Fig. 6 Library of representative electron donor materials used for iOPVs. EH = 2-ethylhexyl, BO = 2-butyloctyl, HD = 2-hexyldecyl, OD = 2-octyldodecyl

proportional to $1 + R_s/R_{sh}$. Hence, under dim-light indoor conditions, R_s/R_{sh} is sufficiently small, and J_{sc} becomes tolerant to the active layer thickness.

Among the renowned donor polymers developed for outdoor solar cells, PBDB-T and its halogenated derivatives (Fig. 6) have demonstrated the highest PCEs, especially when combined with NFAs under 1-sun conditions. Solar cells employing PBDB-TF (*alias* PM6) as the donor delivered record-high PCEs of up to 18% [19]. In 2019, Hou and co-workers reported an impressive indoor photovoltaic performance for the PBDB-TF:$PC_{71}BM$ system in 1 cm^2 cells, achieving a high PCE of 18.1% with V_{oc} of 0.78 V under a 2700 K LED (1000 lx) [62]. By replacing the benzodithiophene dione (BDD) subunit in PBDB-TF with a quinoxaline derivative, Lee and co-workers developed new donor polymers, WF3 and WF3F [63]. While the E_g values of these two polymers are similar in the range of 1.73–1.78 eV, WF3F has a deeper HOMO

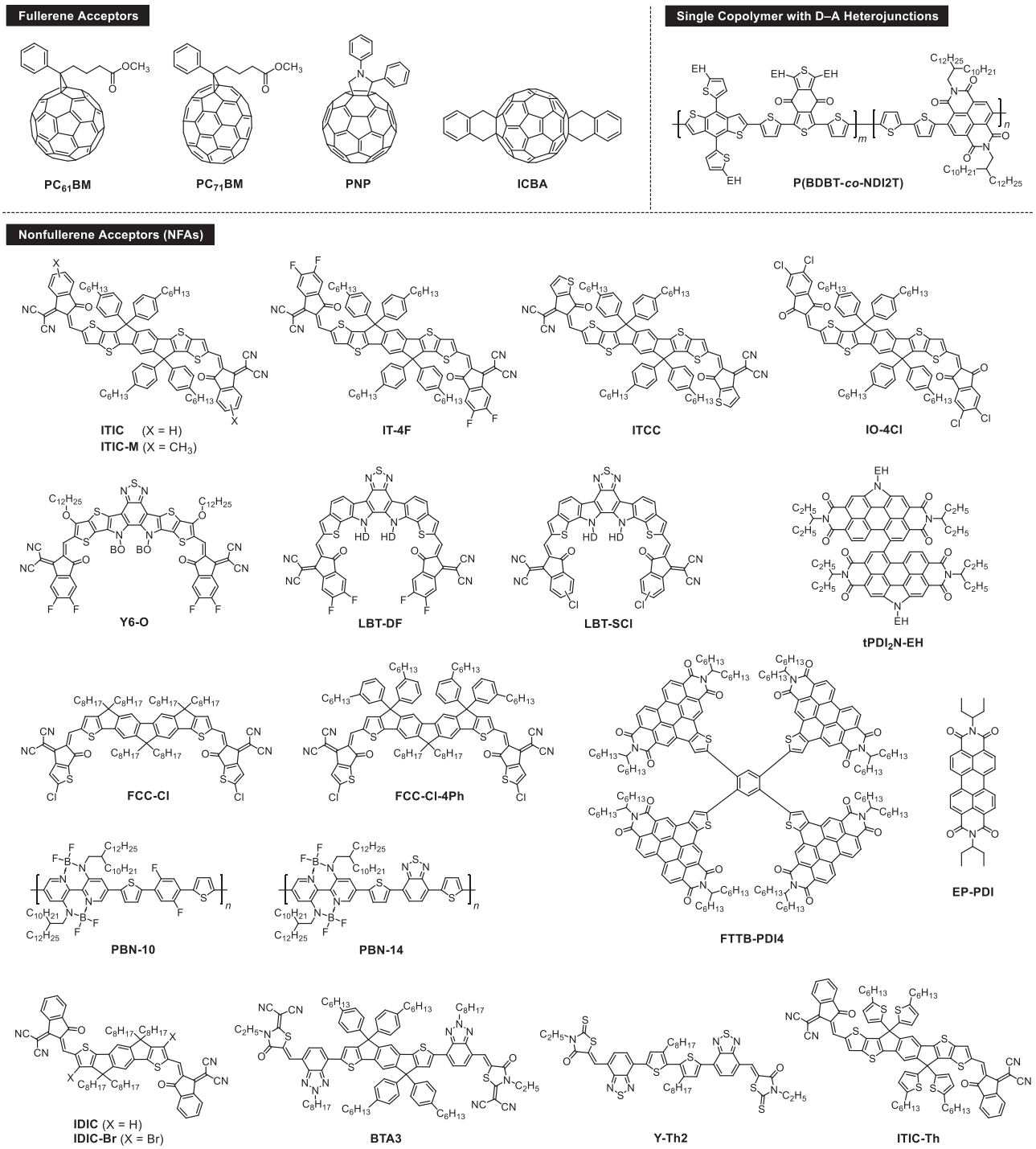

Fig. 7 Library of representative electron acceptor materials used for iOPVs. EH = 2-ethylhexyl, BO = 2-butyloctyl, HD = 2-hexyldecyl

level of −5.62 eV than WF3 because of the additional fluoro substituents. Consequently, the WF3F:$PC_{71}BM$-based iOPV exhibited a higher PCE of 17.1% with V_{oc} of 0.69 V under LED (500 lx), which surpassed that of the WF3:$PC_{71}BM$-based device (PCE = 12.4% and V_{oc} = 0.57 V). It is intriguing that even if the polymer backbones are exactly the same, indoor photovoltaic properties can be significantly altered by a slight difference in the substituents. More recently, PTQ10 [94], which has a reputation as a donor polymer for outdoor solar cells, was reported to exhibit good performance in iOPVs [67]. The PTQ10:$PC_{61}BM$-based iOPVs delivered a high PCE approaching 20% with a V_{oc} of 0.79 V under LED (500 lx). The lower synthetic complexity of

Table 1 Indoor photovoltaic characteristics of representative fullerene-based iOPVs

Donor	Acceptor	L (lx)	P_{in} (μW cm^{-2})	PCE (%)	V_{oc} (V)	J_{sc} (μA cm^{-2})	FF (%)	P_{out} (μW cm^{-2})	Light source	Ref.
Polymer donor–fullerene acceptor binary system										
P3HT	$PC_{61}BM$	500	176	8.9	0.43	62	59	15.6	LED	[53]
P3HT	ICBA	500	176	13.0	0.73	50	63	23.0	LED	[53]
PTB7-Th	$PC_{71}BM$	500	176	13.2	0.59	66	58	23.2	LED	[53]
PTB7-Th	$PC_{71}BM$	890	364	11.6	0.62	92	74	42.3	LED	[48]
PTB7-Th	$PC_{71}BM$	1000	280	16.3	0.63	123	60	46.5	LED	[65]
PTB7	$PC_{71}BM$	300	83.6	14.6	0.61	28.6	70	12.2	FL	[49]
PCDTBT	$PC_{71}BM$	300	83.6	16.6	0.72	27.7	69	13.9	FL	[49]
PCDTBT	$PC_{71}BM$	300	77.6	18.7	0.74	31.1	63	14.5	LED (3000 K)	[57]
PPDT2FBT	$PC_{71}BM$	1000	280	16.0	0.59	117	65	44.9	LED	[59]
PPDT2FBT	$PC_{61}BM$	300	90	13.0	0.59	29.4	68	11.6	LED (2800 K)	[64]
PPDT2FBT	$PC_{61}BM$	1000	310	13.8	0.62	94.6	70	41.3	LED (2800 K)	[64]
PPDT2FBT	$PC_{61}BM$	300	90	11.5	0.58	26.8	67	10.5	LED (5600 K)	[64]
PPDT2FBT	$PC_{61}BM$	1000	310	11.8	0.62	85.0	70	36.7	LED (5600 K)	[64]
PDTBTBz-2F	$PC_{71}BM$	1000	280	23.1	0.82	112	70	64.8	LED	[61]
PBDB-T	$PC_{71}BM$	1000	280	15.3	0.67	90.2	71	42.8	LED	[61]
PBDB-TF (PM6)	$PC_{71}BM$	200	60.4	15.9	0.71	18.9	71	9.6	LED (2700 K)	[62]
PBDB-TF (PM6)	$PC_{71}BM$	1000	302	18.1	0.78	94.1	74	54.7	LED (2700 K)	[62]
WF3	$PC_{71}BM$	500	170	12.4	0.57	58.3	64	21.3	LED	[63]
WF3F	$PC_{71}BM$	500	170	17.1	0.69	63.6	67	29.1	LED	[63]
PTQ10	$PC_{61}BM$	500	180	19.9	0.79	62.5	73	35.8	LED	[67]
SM donor–fullerene acceptor binary systems										
BTR	$PC_{71}BM$	1000	278	28.1	0.79	133	75	78.2	FL	[54]
P1	$PC_{71}BM$	300	77.6	18.7	0.74	31.1	63	14.5	LED (3000 K)	[57]
BDT-1T-ID	PNP	200	76.8	12.4	0.84	19.2	59	9.5	LED (8500 K)	[60]
BDT-2T-ID	PNP	200	76.8	16.0	0.75	24.2	68	12.3	LED (8500 K)	[60]
1DTP-ID	PNP	200	57.9	19.3	0.67	24.6	68	11.2	LED (2900 K)	[35]
1DTP-ID	PNP	200	66.1	17.4	0.67	25.6	67	11.5	LED (5300 K)	[35]
1DTP-ID	PNP	200	70.1	17.7	0.69	26.4	68	12.4	LED (7500 K)	[35]
2DTP-ID	PNP	200	57.9	17.8	0.72	22.8	63	10.3	LED (2900 K)	[35]
2DTP-ID	PNP	200	66.1	13.2	0.74	20.1	59	8.7	LED (5300 K)	[35]
2DTP-ID	PNP	200	70.1	13.8	0.71	22.4	61	9.6	LED (7500 K)	[35]
DTCPB	C_{70}	200	58.0	13.4	0.66	21.7	54	7.8	FL	[68]

L illuminance of incident light, P_{in} input power density (irradiance), *PCE* power conversion efficiency, V_{oc} open-circuit voltage, J_{sc} short-circuit current density, *FF* fill factor, P_{out} output power density

the PTQ10:$PC_{61}BM$ system enables iOPV upscaling in mass-production protocols, including roll-to-roll (R2R) printing.

Small-molecule donor–fullerene acceptor binary systems

Another category of iOPV systems is based on a combination of SM donors and fullerene acceptors. Unlike polymer-based systems, this material class has some inherent advantages, such as well-defined molecular structures, monodispersity, high purity, negligible batch-to-batch variations, and energy-level tunability. Nevertheless, the development of SM donors for iOPVs has lagged behind that for their polymer counterparts. Excellent indoor photovoltaic characteristics have been achieved for some SM donor–fullerene acceptor BHJ systems, as described in this section.

In 2018, Lee et al. demonstrated the first SM-based iOPVs and achieved impressive PCEs of 26.2% at 200 lx

Table 2 Indoor photovoltaic characteristics of representative NFA-based iOPVs

Donor	Acceptor	L (lx)	P_{in} (μW cm^{-2})	PCE (%)	V_{oc} (V)	J_{sc} (μA cm^{-2})	FF (%)	P_{out} (μW cm^{-2})	Light source	Ref.
Polymer donor–NFA binary systems										
PBDB-TF	ITCC	200	60.4	20.4	0.92	19.2	70	12.3	LED (2700 K)	[62]
PBDB-TF	ITCC	500	151	21.2	0.95	47.8	71	32.0	LED (2700 K)	[62]
PBDB-TF	ITCC	500	159	20.4	0.95	48.5	70	32.4	LED (6500 K)	[62]
PBDB-TF	ITCC	1000	302	22.0	0.96	95.8	72	66.5	LED (2700 K)	[62]
PBDB-TF	IT-4F	200	60.4	18.2	0.66	22.8	73	11.0	LED (2700 K)	[62]
PBDB-TF	IT-4F	500	151	19.6	0.69	56.6	76	29.6	LED (2700 K)	[62]
PBDB-TF	IT-4F	1000	302	20.8	0.71	113	78	62.8	LED (2700 K)	[62]
PBDB-TF	IO-4Cl	200	60.4	22.2	1.03	18.2	72	13.4	LED (2700 K)	[28]
PBDB-TF	IO-4Cl	500	151	24.6	1.07	45.1	77	37.1	LED (2700 K)	[28]
PBDB-TF	IO-4Cl	1000	302	26.1	1.10	90.6	79	78.8	LED (2700 K)	[28]
PBTB-TF	Y6-O	290	88.3	28.1	0.79	44.0	71	24.8	LED (3000 K)	[29]
PBTB-TF	Y6-O	700	213	29.5	0.81	102	76	62.8	LED (3000 K)	[29]
PBTB-TF	Y6-O	1200	365	30.0	0.83	175	76	110	LED (3000 K)	[29]
PBDB-TF	ITIC-M	500	158	22.8	0.88	54.2	75	36.0	LED (2700 K)	[78]
PBDB-TSC1	IT-4F	500	135	21.5	0.63	60.4	76	29.1	FL	[72]
PBDB-TSC1	IT-4F	1000	299	20.1	0.66	118	77	59.9	FL	[72]
TPD-3F	IT-4F	1000	185	26.2	0.75	99.5	65	48.5	FL	[74]
S2	LBT-DF	500	159	23.0	0.77	63.4	74	36.6	LED (2600 K)	[86]
S2	LBT-DF	1000	318	24.2	0.80	126	76	76.9	LED (2600 K)	[86]
S2	LBT-SCl	500	159	23.6	0.84	63.2	71	37.7	LED (2600 K)	[86]
S2	LBT-SCl	1000	318	25.1	0.86	125	74	80.0	LED (2600 K)	[86]
PBDB-TF	FCC-Cl	500	159	27.1	0.87	61.1	81	43.1	LED (2600 K)	[85]
PBDB-TF	FCC-Cl	1000	318	27.9	0.89	122	81	88.7	LED (2600 K)	[85]
D18	FCC-Cl	500	159	28.8	0.93	61.6	79	45.8	LED (2600 K)	[85]
D18	FCC-Cl	1000	318	29.4	0.95	123	80	93.5	LED (2600 K)	[85]
D18	FCC-Cl-4Ph	500	145	28.7	0.95	55.8	79	41.6	LED (3000 K)	[92]
D18	FCC-Cl-4Ph	1000	290	29.3	0.97	110	79	85.0	LED (3000 K)	[92]
CD1	ITIC	1000	345	17.9	0.78	116	68	62.0	FL	[75]
CD1	ITIC	1000	360	15.4	0.77	107	68	56.0	LED	[75]
CD1	PBN-10	1000	345	26.2	1.14	120	66	91.0	FL	[75]
CD1	PBN-10	1000	360	21.7	1.14	105	65	78.0	LED	[75]
CD1	PBN-14	1000	345	22.9	1.07	116	63	79.0	FL	[83]
CD1	PBN-14	1000	360	21.4	1.06	116	63	77.0	LED	[83]
PPDT2FBT	ITIC-M	300	90	6.9	0.53	20.8	57	6.3	LED (5600 K)	[64]
PPDT2FBT	ITIC-M	1000	310	7.5	0.62	68.5	55	23.2	LED (5600 K)	[64]
PPDT2FBT	tPDI$_2$N-EH	300	90	9.0	0.79	20.9	50	8.2	LED (5600 K)	[64]
PPDT2FBT	tPDI$_2$N-EH	1000	310	8.9	0.84	65.4	50	27.6	LED (5600 K)	[64]
P3TEA	FTTB-PDI4	170	52	24.2	0.94	20.9	64	12.6	LED (3000 K)	[66]
P3TEA	FTTB-PDI4	1010	311	23.9	1.00	111	67	74.4	LED (3000 K)	[66]
PBDB-T	BTA3	500	152	23.3	0.95	51.7	69	33.8	LED (2700 K)	[87]
PBDB-T	BTA3	1000	307	22.2	0.99	98.5	74	71.8	LED (2700 K)	[87]
PTQ10	IDIC	600	150	16	0.79	53	57	24	LED	[91]
PTQ10	IDIC-Br	600	150	19	0.70	64	62	28	LED	[91]
Single copolymer system										
P(BDBT-*co*-NDI2T)		500	170	12.7	0.71	49.9	61	21.6	LED	[80]

Table 2 (continued)

Donor	Acceptor	L (lx)	P_{in} (μW cm^{-2})	PCE (%)	V_{oc} (V)	J_{sc} (μA cm^{-2})	FF (%)	P_{out} (μW cm^{-2})	Light source	Ref.
Ternary and quaternary systems										
PCDTBT:PDTSTPD	$PC_{71}BM$	300	77.6	18.1	0.72	31.4	62	14.1	LED (3000 K)	[55]
PTB7	$PC_{71}BM$:EP-PDI	500	170	15.4	0.65	57	69	26	LED	[69]
PBDB-T	$PC_{71}BM$:ITIC-Th	200	55	25.6	0.65	32.1	68	14.1	LED	[71]
PBDB-T	$PC_{71}BM$:ITIC-Th	1000	280	26.4	0.72	158	65	73.9	LED	[71]
PBDB-T:PTB7-Th	$PC_{71}BM$	1000	280	19.0	0.63	158	54	53.2	LED	[71]
PM6	Y6:Y-Th2	1000	730	22.3	0.70	320	74	163	Solar LED	[76]
OD	$PC_{71}BM$:IDT	1000	280	21.1	0.63	133	72	59.2	LED	[77]
PPDT2FBT	$PC_{61}BM$:$tPDI_2N$-EH	1000	288	14.6	0.69	87	70	42.1	LED (2700 K)	[81]
J52-F:PM7	BTA3	300	90	20.0	1.00	26.5	68	18	LED (3000 K)	[82]
PBDB-T:PTB7-Th	$PC_{71}BM$:ITIC-Th	1000	280	14.3	0.68	102	57	40	LED	[70]
PM6:PTB7-Th	$PC_{71}BM$:ITIC-Th	1000	300	25.0	0.77	122	80	74.9	LED (3000 K)	[93]

L illuminance of incident light, P_{in} input power density (irradiance), *PCE* power conversion efficiency, V_{oc} open-circuit voltage, J_{sc} short-circuit current density, *FF* fill factor, P_{out} output power density

and 28.1% at 1000 lx under FL illumination [54] (note that the light source was different from general LEDs). In this system, BTR (Fig. 6) [95] was used as the SM donor, in combination with the $PC_{71}BM$ acceptor. The deep-lying HOMO of BTR ($E_{HOMO} = -5.34$ eV) enabled a high V_{oc} of 0.95 V under 1-sun conditions and 0.79 V under indoor conditions, resulting in a rather small V_{oc} reduction (<0.2 V). Yin et al. developed a porphyrin-based SM donor P1 for iOPVs [57]. Under LED illumination (300 lx), the P1:$PC_{71}BM$-based iOPVs exhibited PCEs as high as 19.1%, outperforming the PCDTBT:$PC_{71}BM$-based devices (PCE = 18.7%). Furthermore, the P1:$PC_{71}BM$ system showed remarkable thickness tolerance; a device with a thicker photoactive layer (~200 nm) exhibited a comparable PCE of 18.4% under the same conditions, owing to the reduced energetic defects or disorders.

In 2019, Yasuda and co-workers reported promising indoor photovoltaic functionality for the new SM donors, BDT-1T-ID and BDT-2T-ID (Fig. 6) [60, 96], which possess ideal E_gs of 1.7–1.8 eV and deep-lying HOMOs of −5.23 and −5.13 eV, respectively. The BDT-1T-ID:PNP- and BDT-2T-ID:PNP-based devices demonstrated higher PCEs of 12.4% and 16.0% (with V_{oc}s of 0.84 and 0.75 V, respectively) under LED (200 lx) compared to those measured under 1-sun illumination (PCE = 3.6% and 5.8%, respectively). Furthermore, the BDT-2T-ID:PNP-based device demonstrated stable PCEs over a wide illuminance range of 200–10000 lx, retaining high values exceeding 16%. These almost illuminance-independent PCE characteristics make SM-based iOPVs more attractive and reliable for practical applications. Indeed, by adopting the BDT-2T-ID:PNP system, six series-connected flexible iOPV modules were successfully produced, which are capable of generating a high output power over 100 μW and high V_{oc} of 4.2 V even under 200 lx dim-light conditions (see Section "iOPV modules for practical applications" for details). This achievement opens a new avenue for preparing dispersive self-sustainable electric power sources.

Following a design strategy aimed at HOMO deepening, the same group subsequently developed new SM donors, 1DTP-ID and 2DTP-ID, by incorporating electron-withdrawing π-fused lactam (DTP) subunits [35]. 1DTP-ID and 2DTP-ID have E_gs of 1.65 and 1.70 eV and E_{HOMO}s of −5.25 and −5.35 eV, respectively, which are well suited for iOPVs. Under a warm-white LED (2900 K, 200 lx), the 1DTP-ID:PNP- and 2DTP-ID:PNP-based iOPVs achieved PCEs as high as 19.3% and 17.8%, with V_{oc}s of 0.67 and 0.72 V, respectively. Additionally, important insight into the color-temperature dependence of the LED sources was obtained with this iOPV system (Fig. 8). Artificial white LED power spectra typically comprise sharp blue emission from GaN/InGaN and broad yellow emission from phosphors (Ce:YAG). Cool-white LED light with a high color temperature (~7000 K) has a relatively high ratio of blue light intensity, whereas warm-white LED light with a low color temperature (~3000 K) is dominated by long wavelength emissions (Fig. 8a). Such differences in the spectral irradiance characteristics of the LED sources significantly affect spectral matching with the organic photoactive layers in iOPVs, which causes variations in the resulting PCEs and P_{out} values. As shown by the incident photon-to-electron conversion efficiency (IPCE) spectra (Fig. 8b), the photoactive layers exhibited the most efficient photoresponses in the range of 500–700 nm. Therefore, the corresponding devices showed a strong tendency to exhibit higher PCEs

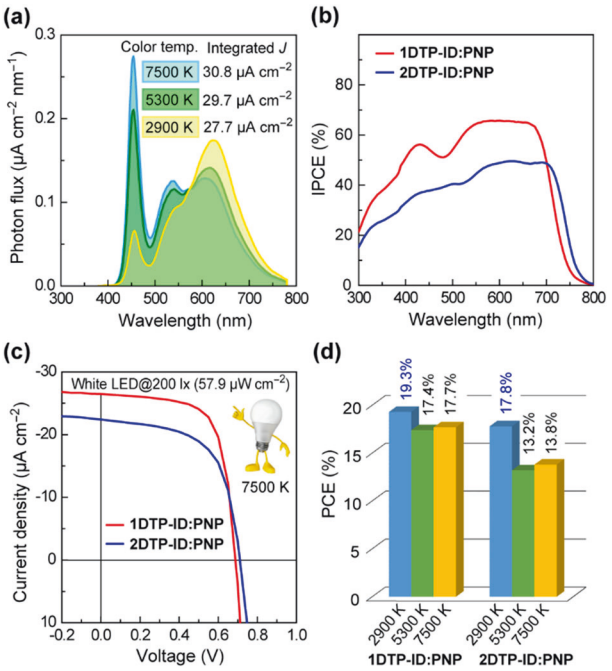

Fig. 8 **a** Emission spectra of white LED light sources with different color temperatures. **b** IPCE spectra and **c** *J*–*V* curves (measured at 200 lx and 7500 K) of the iOPVs based on 1DTP-ID:PNP and 2DTP-ID:PNP. **d** LED color-temperature dependence of PCEs of the iOPVs. Reproduced from reference [35] with permission from Royal Society of Chemistry

under warm-white LED illumination (Fig. 8d and Table 1), where spectral matching was more favorable.

As mentioned earlier, to properly evaluate iOPVs, it is crucial to clarify the color temperature, emission spectrum, and irradiance of the indoor light source. To avoid overestimating and underestimating the intrinsic indoor photovoltaic performance, it is preferable to evaluate iOPVs using a standard natural-white LED with a color temperature of approximately 5000 K, which corresponds to common office and store lighting.

Polymer donor–NFA binary systems

Over the past few years, the performance of fullerene-based iOPVs has steadily improved, with PCEs exceeding 20%, and practical iOPV modules have been successfully developed. However, fullerene-based iOPVs have limited potential for further enhancement of their PCEs because the limited energy-level tunability and visible absorptivity of fullerene acceptors make it difficult to boost V_{oc} and J_{sc}. In contrast, NFAs [44–47] offer opportunities to improve V_{oc} and J_{sc} owing to their adjustable (designable) energy levels, optical E_g, and absorptivity. Since 2019, many research groups have reported the indoor photovoltaic properties of polymer donor–NFA binary systems [28, 29, 62, 64, 66, 69–92], the performance data for which are summarized in Table 2.

ITIC [97] and its derivatives (Fig. 7), which are based on the electron-donating dithieno[2,3-d:2′,3′-d′]-s-indaceno[1,2-b:5,6-b′]thiophene (DTIDT) π-core end-capped with electron-accepting 3-dicyanomethylene-1-indanone groups, are renowned NFAs commonly used in organic solar cells. Owing to the steric hindrance of the side chains, excessive self-aggregation of the seven-ring-fused donor moieties can be suppressed to form suitable nanosegregated BHJ structures. In 2019, Hou and co-workers reported the indoor photovoltaic performance of representative NFAs, IT-4F and ITCC, in combination with PBDB-TF as a polymer donor [62]. The PBDB-TF:ITCC-based iOPVs achieved high PCEs of 20.4–22.0% with high V_{oc}s of 0.92–0.96 V under LED illumination (2700 K, 200–1000 lx), outperforming the PBDB-TF:IT-4F-based devices (PCE = 18.2–20.8% and V_{oc} = 0.66–0.71 V). This result is mainly attributable to the better spectral matching and higher V_{oc} of the PBDB-TF:ITCC system. As shown in Fig. 9, ITCC has a wider optical bandgap (E_g = 1.67 eV) along with shallower LUMO level (E_{LUMO} = −3.76 eV) compared to IT-4F (E_g = 1.50 eV and E_{LUMO} = −4.14 eV), thus leading to both better spectral matching with warm-white LED lighting and increase of V_{oc} in iOPVs. The same group specifically developed a new wider-bandgap NFA for iOPVs, named IO-4Cl (Fig. 7), by employing 5,6-dichloro-indene-1,3-dione as the end-capped group [28]. By combining IO-4Cl (E_g = 1.80 eV) with PBDB-TF (E_g = 1.82 eV), the BHJ system exhibited optimal absorption that matched the emission spectrum of a warm-white LED. Under AM 1.5 G conditions, the PBDB-TF:IO-4Cl-based device afforded a PCE of 9.8% with an exceptionally high V_{oc} of 1.24 V along with a small energy loss ($E_{loss} = E_g - qV_{oc}$) of <0.6 eV. Reflecting this feature, high V_{oc}s of 1.03–1.10 V were maintained under LED illumination (2700 K, 200–1000 lx), thereby resulting in notably high PCEs of 22.2–26.1%. Moreover, the PBDB-TF:IO-4Cl-based iOPV maintained its initial PCE for 1000 h under continuous LED illumination, demonstrating great stability for practical applications.

Although the narrow-bandgap IT-4F would not be an optimal NFA for iOPVs, as described above, reasonably high PCEs can be obtained by combining it with more appropriate donor polymers. In 2019, Son and co-workers developed a new donor polymer, PBDB-TSCl (Fig. 6), by modifying PBDB-TF to better match IT-4F [72, 73]. PBDB-TSCl has a slightly deeper E_{HOMO} (−5.61 eV) than PBDB-TF, resulting in an increase in V_{oc}. The PBDB-TSCl:IT-4F-based iOPV exhibited a higher PCE (21.5%) than the corresponding PBDB-TF:IT-4F-based device (15.6%) under 500 lx FL illumination. Additionally, chlorinated PBDB-TSCl presented higher morphological stability than fluorinated PBDB-TF under thermal stress; after heating at 100 °C for 34 h, the PBDB-TSCl-based device lost only 5% of its initial PCE, while the PCE of the

PBDB-TF-based device was reduced by 25%. At approximately the same time, Facchetti and co-workers reported a new medium-bandgap donor polymer, TPD-3F, for iOPVs [74]. Incorporating an electron-accepting thieno[3,4-c]pyrrole-4,6-dione (TPD) unit renders TPD-3F with a deeper E_{HOMO} of −5.62 eV and wider E_g of 1.90 eV compared to those of PBDB-TF. Consequently, the TPD-3F:IT-4F-based iOPV demonstrated a PCE as high as 26.2% under FL illumination.

In 2020, Yan and co-workers reported high-efficiency iOPVs using PBDB-TF (*alias* PM6) as the donor in combination with a new NFA, Y6-O [29]. Y6-O was designed by replacing the two alkyl groups of Y6 with alkoxy groups and exhibits upshifted HOMO and LUMO levels as well as blue-shifted absorption compared to Y6 [98]. The PM6:Y6-O-based iOPVs incorporating PDI-NO as an electron transport layer (ETL) achieved record-high PCEs of over 30% with a high V_{oc} of 0.83 V and a FF of 76% under LED illumination (3000 K, 1200 lx). As shown in Fig. 10, the choice of ETL is critically important for device performance. Both the PM6:Y6-O-based devices with PDI-NO and PFN as the ETL showed very similar performance under 1-sun (AM 1.5 G) conditions (Fig. 10b). However, under indoor conditions, the PDI-NO-containing device exhibited better performance than the PFN-containing device over a wide illuminance range (170–1650 lx). This difference can be explained by the work function (WF) shift at the ETL/Al interface. Upon Al modification with PDI-NO ($E_{HOMO} = -6.21$ eV), the WF downshifted from 4.22 to 3.97 eV, while it shifted from 4.22 to 4.12 eV with PFN ($E_{HOMO} = -5.61$ eV). Although both ETLs can reduce the WF of Al to form ohmic contacts with the acceptor and improve electron extraction, the energy difference (Δh) between the E_{HOMO} of the ETL and the Fermi level (E_F) of Al, which represents the hole-blocking barrier, is clearly different for the respective devices (2.31 eV for PDI-NO and 1.49 eV for PFN). Compared with the PFN-containing device, the PDI-NO-containing device showed a lower leakage current and higher R_{sh} (similar R_s) because of its good hole-blocking ability (large Δh), thus leading to higher V_{oc} and FF, even under dim-light conditions (Fig. 10c). In this way, not only optimization of the donor–acceptor combinations but also interfacial engineering is of vital importance for improving iOPV performance.

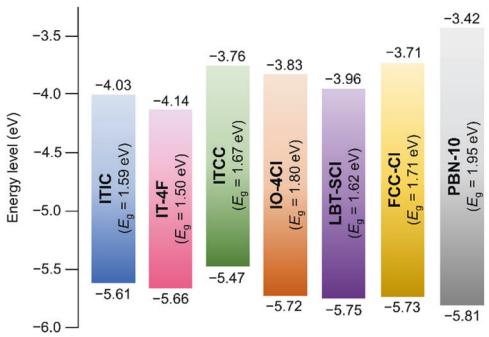

Fig. 9 Energy-level diagram for representative nonfullerene acceptors. E_g = optical bandgap

In seeking to enlarge the optical E_g and upshift the E_{LUMO} of Y6, in 2021, the same group developed the medium-bandgap NFAs, LBT-DF and LBT-SCl (Fig. 7), by replacing the fused thieno[3,2-*b*]thiophene subunit of Y6 with benzothiophene [86]. The E_gs of LBT-DF and LBT-SCl are 1.64 and 1.62 eV, respectively, and therefore, their absorption spectra, which cover 500–750 nm, are more compatible with indoor lighting than that of Y6. iOPVs based on S2:LBT-DF and S2:LBT-SCl blends achieved high PCEs of 23.0–25.7% and 23.6–27.3%, respectively, under a 2600 K LED with an illuminance range of 500–2000 lx. The same group also developed FCC-Cl and its analogs based on a fluorenedicyclopentathiophene (FDCT) π-core as new medium-bandgap NFAs for iOPVs [85, 92]. FCC-Cl with an E_g of 1.71 eV was combined with two widely used donor polymers (PBDB-TF and D18), and both BHJ systems showed rather high PCEs of 25–30% under a 2600 K LED at 100–2000 lx.

Various new NFAs, which are distinct from the fused-ring ITIC and Y series NFAs, have recently been developed and utilized for iOPVs. In 2019, Liu and co-worker reported that polymer acceptors (PBN series, Fig. 7) featuring boron–nitrogen coordination (B ← N) bonds exhibited excellent indoor photovoltaic properties in combination with a wide-bandgap polymer, CD1, as the donor [75, 83, 89]. Benefitting from the medium optical bandgap of PBN-10 (E_g = 1.95 eV) and good energy-level alignment, all-polymer iOPVs based on the CD1:PBN-10 system exhibited high PCEs of 26.2% and 21.7% with a markedly high V_{oc} of 1.14 V under 1000 lx FL and LED illumination, respectively [75] (Table 2). To date, this is the highest V_{oc} value reported for iOPVs under dim-light conditions, indicating the high potential of all-polymer iOPVs. Meanwhile, for the CD1:ITIC-based device, a large E_{LUMO} offset between CD1 and ITIC resulted in a much lower V_{oc} of 0.77 V and thereby lower PCE of 15.4%.

Another choice for NAFs is a perylene diimide (PDI)-based material. In 2019, Welch and co-workers designed $tPDI_2N$-EH (Fig. 7) as a PDI-based NFA and compared its performance with those of $PC_{61}BM$, ITIC-M, and IT-4F in iOPVs [64]. $tPDI_2N$-EH has a relatively wide E_g (2.22 eV) with photoabsorption in the range of 400–600 nm, which is complementary to the photoabsorption of the donor polymer PPDT2FBT. The PPDT2FBT:$tPDI_2N$-EH-based device exhibited a low PCE of 6.5%, despite its high V_{oc} of over 1 V under 1-sun illumination. However, its PCE increased to 9.0% under LED (5600 K, 300 lx), which is higher than those of the iOPVs using ITIC-M and IT-4F as NFAs. It is

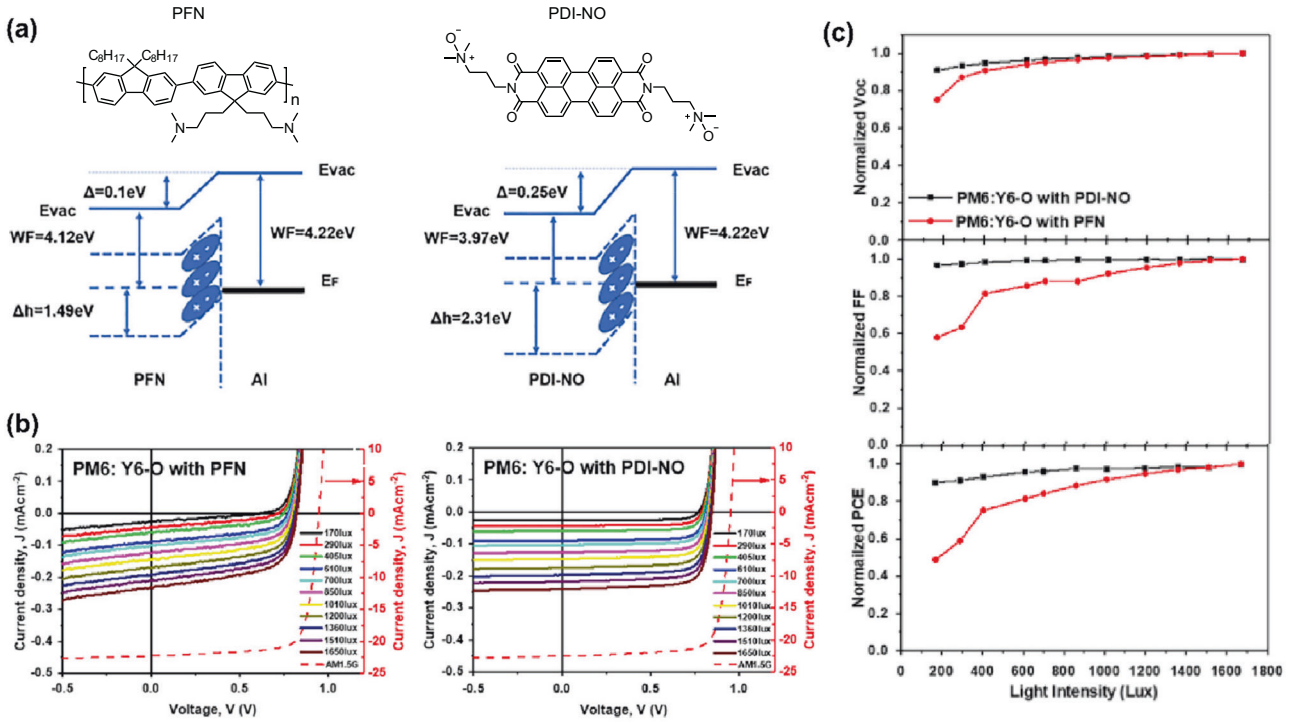

Fig. 10 **a** Energy level alignments between the electron-transporting layer (PFN and PDI-NO) and Al representing the band-bending phenomenon. **b** *J*–*V* curves for the PM6:Y6-O-based devices with PFN and PDI-NO interlayers under AM 1.5 G and indoor LED illumination. **c** Illuminance dependence of photovoltaic parameters (V_{oc}, FF, and PCE) for the PM6:Y6-O-based devices with PFN or PDI-NO interlayers. Reproduced from reference [29] with permission from Elsevier

also noteworthy that these iOPVs can be manufactured by slot-die coating using nonhalogenated solvents (*o*-xylene/diphenyl ether). Yan and co-workers introduced another PDI-based wide-bandgap NFA, FTTB-PDI4, for iOPVs [29, 66]. The P3TEA:FTTB-PDI4 system, which features a near-zero energy offset for the LUMOs, enabled small voltage loss and thereby high V_{oc}. Consequently, the P3TEA:FTTB-PDI4-based iOPVs achieved remarkable PCEs of 23.7–24.2% with high V_{oc}s of 0.94–1.0 V over a wide range of illuminance (170–1650 lx) under a 3000 K LED [66]. Additionally, even with thick active layers (~200 nm), the devices maintained high PCEs of over 21%.

In 2020, Choi and co-workers designed a novel conjugated copolymer, P(BDBT-*co*-NDI2T), possessing donor–acceptor heterojunctions to achieve efficient indoor photovoltaic function using only a single copolymer [80]. Intriguingly, the P(BDBT-*co*-NDI2T)-based iOPVs exhibited higher PCEs (11.1–12.7%) and operational stabilities under LED illumination (200–1000 lx) than devices based on the corresponding binary blends of PBDBT and PNDI2T (PCE = 6.5–6.9%).

Ternary and quaternary systems

Adding a third or fourth component to the binary active layer to construct multi-component BHJ systems with improved photoabsorption, morphology, and charge-transport properties is a feasible and effective strategy for fabricating iOPVs with improved performance. As summarized in Table 2, the ternary systems consist of either D1:D2:A (dual donors/single acceptor) [55, 71, 82] or D:A1:A2 (single donor/dual acceptors) compositions [69, 71, 76, 77, 81], whereas the quaternary systems are entirely based on D1:D2:A1:A2 (dual donors/dual acceptors) compositions [70, 93].

In 2018, So and co-workers demonstrated the first effective ternary BHJ system for iOPVs [55]. By introducing the donor polymer PDTSTPD as the third component into the binary PCDTBT:$PC_{71}BM$ system, the PCEs increased from 16.0% (binary) to 18.1% (ternary) under LED illumination (3000 K, 300 lx). Blending of (PDTSTPD) can passivate shallow traps near the band edges of the BHJ and improve the charge transport properties, leading to an improvement in the PCE. Similarly, Lee and co-workers introduced a PDI-based SM acceptor (EP-PDI) as a third component into a binary PTB7:$PC_{71}BM$ system [69]. The optimal PTB7:$PC_{71}BM$:EP-PDI-based device showed an improved PCE of 15.4% under LED illumination at 500 lx compared to the binary PTB7:$PC_{71}BM$-based device (PCE = 8.9%).

Ko and co-workers conducted a comparative study of D1:D2:A and D:A1:A2 ternary blends consisting of PBDB-T:PTB7-Th:$PC_{71}BM$ and PBDB-T:$PC_{71}BM$:ITIC-Th [71].

Although both systems were universally effective, the D:A1:A2 system incorporating an NFA (ITIC-Th) benefited from less charge recombination and higher PCEs. Consequently, the optimized ternary PBDB-T:$PC_{71}BM$:ITIC-Th-based iOPVs showed better performance, with PCEs of 25.6% and 26.4% under LED illumination at 200 and 1000 lx, respectively. In this system, the third NFA additive, ITIC-Th, self-organized at the PBDB-T:$PC_{71}BM$ interface to form effective cascade ternary junctions, resulting in less charge recombination. Moreover, the ternary PBDB-T:$PC_{71}BM$:ITIC-Th-based iOPVs showed superior thermal durability and retained ~90% of their initial PCEs after heating at 60 °C for 100 h. This feature would be crucial as iOPVs move forward toward practical applications.

Yang and co-workers newly synthesized a non-fused 2,2'-bithiophene-based NFA, Y-Th2, and introduced it into a PBDB-TF:Y6 system to construct ternary iOPVs with cascade energy-level alignment [76]. Owing to its wider optical bandgap ($E_g = 1.74$ eV), Y-Th2 complemented the absorption spectra of PM6 and Y6 in the relatively short wavelength region with high absorptivity. Consequently, impressive indoor photovoltaic performance with PCEs of up to 22.3% was obtained for the ternary PM6:Y6:Y-Th2-based iOPV under a solar LED (1000 lx).

In addition, several iOPVs featuring quaternary BHJ systems have been reported. In 2019, Ko and co-workers successfully demonstrated quaternary iOPVs composed of two polymer donors (PBDB-T and PTB7-Th) and two SM acceptors ($PC_{71}BM$ and ITIC-Th) [70]. Compared to their corresponding binary counterparts (PBDB-T:$PC_{71}BM$ and PTB7-Th:ITIC-Th), the quaternary BHJ system benefitted from broadened spectral response, enhanced charge transport, and improved morphological stability. Consequently, the quaternary PBDB-T:PTB7-Th:$PC_{71}BM$:ITIC-Th-based iOPVs achieved an improved PCE of 14.3% under LED illumination (1000 lx). This quaternary system also presented a semitransparent feature without impairing the high PCEs. More recently, to fabricate high-performance quaternary iOPVs, the same group introduced sequential deposition based on consecutive spin-coating of two binary donor/acceptor blends [93]. To form a desirable quaternary BHJ layer, the first blend solution (PTB7-Th:ITIC-Th) was spin-coated onto a ZnO-coated indium-tin-oxide (ITO) substrate, and then the second blend solution (PM6:$PC_{71}BM$) was promptly spin-coated onto the first blend layer. The sequentially processed quaternary iOPV exhibited superior performance with a PCE of 25.0% under LED (3000 K, 1000 lx) compared to the binary PM6:$PC_{71}BM$-based device (PCE = 19.9%).

iOPV modules for practical applications

As outlined in the above sections, the performance of iOPVs has drastically improved in a short period of time and is now reaching practicality as a promising energy harvesting technology. The inherent flexibility, light weight, and applicability to a variety of solution-based manufacturing techniques (such as spin coating, slot-die coating, inkjet printing, and R2R printing) [99] make iOPVs attractive for indoor applications. Development of large-area devices and modules is essential for practical use of the iOPVs. This section briefly introduces the research achievements for state-of-the-art iOPV modules composed of series-connected unit cells, the performance data for which are summarized in Table 3.

In 2016, Lee et al. successfully fabricated iOPV modules (eight cells in series) based on PCDTBT:$PC_{71}BM$ with a total active area of 100 cm^2 and achieved a module PCE of 11.2% (with $V_{oc} = 4.87$ V, $I_{sc} = 314$ μA, and FF = 61%), generating a maximum power (P_{out}) of 938 μW under a 300 lx FL illumination (Fig. 11a) [49]. In 2020, a module PCE exceeding 20% was achieved by Facchetti and co-workers [74]. The iOPV modules (five cells in series) based on TPD-3F:IT-4F fabricated by blade coating exhibited an outstanding PCE of 21.8% (with $V_{oc} = 3.21$ V, $I_{sc} = 361$ μA, and FF = 71%) under 1000 lx FL (Fig. 11b). The present modules also performed well as solar cells under 1-sun (AM 1.5 G) conditions, yielding a PCE of 10.4% ($V_{oc} = 4.45$ V, $I_{sc} = 78.7$ mA, and FF = 61%). The potential for dual use in indoor and outdoor environments is highly attractive and offers great practicality and additional value.

iOPV modules with high mechanical flexibility and bendability are ideal energy harvesters because such devices can be installed anywhere, including curved walls and narrow crevices. High-performance flexible iOPV modules were first demonstrated by Yasuda and co-workers (Fig. 11c, d) [35, 60]. They fabricated BDT-2T-ID:PNP-based iOPV modules (six cells in series) with a total active area of 9.5 cm^2 on a rigid glass substrate and on a flexible polyethylene naphthalene (PEN) substrate, and these modules exhibited high PCEs of 20.2% and 18.4%, respectively, delivering P_{out} as high as 111 and 101 μW under LED illumination at 200 lx. The same group also developed similar flexible iOPV modules based on 1DTP-ID:PNP, achieving a comparatively high module PCE of 17.0% ($V_{oc} = 4.05$ V, $I_{sc} = 35.1$ μA, and FF = 67%) [35]. In these six series-connected modules, the average value of V_{oc} for each sub cell was consistent with the V_{oc} of a single test cell. Therefore, upscaling and modularization without lowering V_{oc} and FF enable a high P_{out} and PCE under indoor conditions.

Summary and outlook

In this review, we have summarized recent progress in emerging iOPV technologies. Full-fledged iOPV research

Table 3 Performance data for representative iOPV modules

Donor	Acceptor	A (cm^2)	L (lx)	P_{in} (μW cm^{-2})	PCE (%)	V_{oc} (V)	I_{sc} (μA)	FF (%)	P_{out} (μW)	Light source	Ref.
PCDTBT	$PC_{71}BM$	100	300	83.6	11.2	4.87	314	61	938	FL	[49]
TPD-3F	IT-4F	20.4	1000	185	21.8	3.21	361	71	818	FL	[74]
CD1	PBN-21	10	1000	305	12.0	4.20	157	56	367	LED	[89]
BDT-2T-ID	PNP	9.5	200	57.9	20.2	4.20	39.9	66	111	LED (2900 K)	[60]
1DTP-ID	PNP	9.6	200	57.9	17.0	4.05	35.1	67	95.4	LED (2900 K)	[35]

A effective active area, *L* illuminance of incident light, P_{in} input power density (irradiance), *PCE* power conversion efficiency, V_{oc} open-circuit voltage, I_{sc} short-circuit current, *FF* fill factor, P_{out} output power.

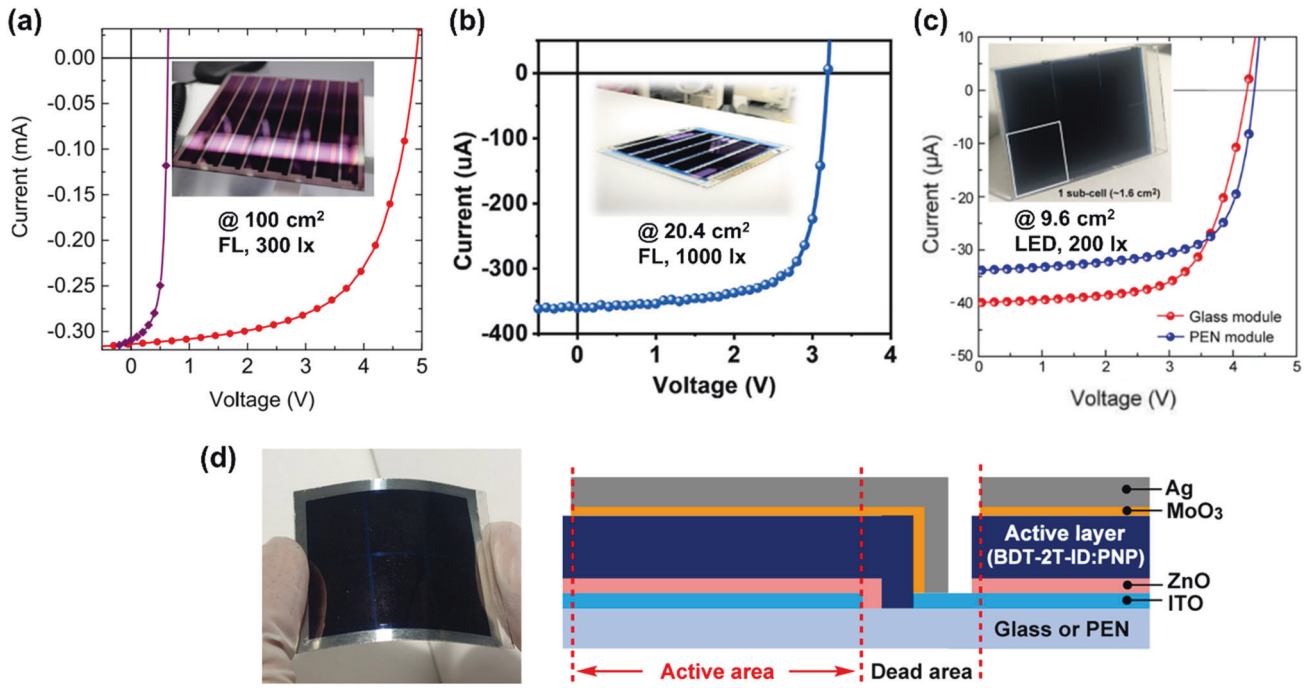

Fig. 11 Appearance and current–voltage (*I–V*) characteristics of large-area iOPV modules based on (**a**) PCDTBT:$PC_{71}BM$ [49], (**b**) TPD-3F:IT-4F [74], and (**c**) BDT-2T-ID:PNP [60]. **d** A photograph of the six series-connected flexible iOPV modules based on BDT-2T-ID:PNP ($A = 9.5\ cm^2$) fabricated on a PEN substrate (left) and schematic cross-sectional drawing for the basic module design [60]. Reproduced from references [49, 60] with permission from AIP Publishing, Elsevier, and American Chemical Society

began a few years ago, and many challenges must be overcome for practical use. Although much of the knowledge accumulated for outdoor organic solar cells can be used as a reference for developing iOPVs, they require different design strategies in terms of both materials chemistry and device physics. This difference primarily originates from the different emission spectra and intensities of the light sources used (i.e., sunlight *vs*. indoor LED lighting). Unlike solar cells, because only visible light ranging from 400 to 750 nm is available in iOPVs, their photoactive layers based on organic semiconductors should have wider optical bandgaps. Theoretical simulations predict that the optimal bandgap for iOPVs under white LED illumination is 1.7–1.9 eV and the SQ-limited maximum PCE is as high as ~57% [40]. Therefore, the key to improving iOPV performance is to design and apply appropriate organic semiconductors that enable good spectral matching with white LEDs as an incident light source.

However, the current problem is that the light sources are not standardized; therefore, establishing appropriate evaluation methodologies for iOPVs is an urgent task. It is crucial to specify the color temperature, emission spectrum, and irradiance of an indoor light source for iOPV measurements. In general, warm-white LED light with a color temperature of approximately 3000 K tends to afford a higher PCE owing to its superior spectral matching with common iOPVs. Because the PCEs and output power densities vary depending on the color temperature of the light source, it is recommended that iOPVs should be evaluated with a standard natural-white LED with a color temperature of approximately 5000 K, thus enabling fair comparisons of the results reported by different groups.

Additionally, many previous iOPV studies have reported results obtained only at 1000 lx or even higher, which typically leads to higher PCEs than under lower illuminance; however, this cannot be representative of indoor energy harvesters. Hence, measurements under lower illuminance (200–500 lx), in addition to 1000 lx, are recommended to obtain a better illustration of the actual indoor photovoltaic performance.

From the device design perspective, the most important point is how to suppress V_{oc} reduction under low illuminance. A key strategy with which to overcome this challenge is to maximize the R_{sh} of the device as much as possible. As discussed in Section "Polymer donor–NFA binary systems", introduction of a hole-blocking/electron-transporting layer is a viable and effective approach to increasing R_{sh} by suppressing carrier leakage, thereby enhancing V_{oc} and PCE under dim-light conditions [29]. Additionally, the use of a thicker BHJ active layer can reduce the leakage current (J_0) and increase the R_{sh} of iOPVs [50, 59, 66, 67, 85]. However, considering the recombination losses of carriers and excitons, long propagation paths in these thick active layers may not be a favorable strategy in some cases. In summary, high-efficiency iOPVs can be achieved by (i) optimizing the bandgaps of organic semiconductors (donors and acceptors) to match the indoor light emission spectrum, (ii) constructing BHJ systems with the highest possible V_{oc} (with low voltage loss), and (iii) designing materials and devices with sufficiently large R_{sh} and minimized leakage current.

Currently, the PCEs of state-of-the-art iOPVs have surpassed 30% under indoor conditions, resulting in power outputs of approximately 25, 63, and 110 μW at 290, 700, and 1200 lx, respectively [29]. These efficiencies seem to be sufficiently high for practical application of iOPVs, but from a scientific perspective, there is still room for improvement up to the SQ limit, as mentioned above. Thus, we expect that synergistic advances in basic physical research on exciton/carrier dynamics under low illuminance and state-of-the-art materials and device engineering will further improve the PCEs of iOPVs.

Another critical factor for practical application is the stabilities and durabilities of the devices. Ultimately, to replace the battery market for IoT ecosystems, highly stable iOPVs that can maintain over 80% of their initial efficiencies in indoor environments for several years are desired. Owing to the absence of UV light and the relatively low light intensity, iOPVs have shown better stability under indoor LED lighting than under 1-sun illumination [28], which can overcome the shortcomings related to the photostabilities of organic materials. However, the stabilities of iOPVs under elevated temperature, humidity, and oxygen conditions have rarely been studied; thus, additional systematic investigations are necessary to ensure comprehensive device stability for practical application. We envision that, compared to the harsh outdoor conditions with drastic fluctuations in solar irradiation, heating, and weather, operation under relatively mild indoor conditions will offer a promising route for sufficiently prolonged device durability for iOPVs.

As the next target of iOPV research, upscaling, modularization, and integration of devices should be highlighted to find real industrial markets. Nevertheless, to date, only a few achievements have been reported for practical iOPV modules (especially flexible modules) [35, 49, 52, 60, 74, 89]. A process shift from spin coating to innovative printing techniques compatible with large-scale, low-cost manufacturing is necessary to produce practical iOPV modules. The unique features of iOPVs based on organic semiconductors can increase the freedom of design, shapes, colors, and transparency of actual devices, thereby facilitating their integration into real IoT applications. With rapid advances in both materials and devices, iOPVs will realize their full potential for commercialization in the near future.

Acknowledgements This work was supported in part by a Grant-in-Aid for Adaptable and Seamless Technology Transfer Program through Target-driven R&D (A-STEP) from JST (Grant No. JPMJTR201B for TY), JSPS KAKENHI (Grant No. 21K20431 for SH), and the Hirose Foundation (SH).

Compliance with ethical standards

Conflict of interest The authors declare no competing interests.

Publisher's note Springer Nature remains neutral with regard to jurisdictional claims in published maps and institutional affiliations.

References

1. Lim H-R, Kim HS, Qazi R, Kwon Y-T, Jeong J-W, Yeo W-H. Advanced soft materials, sensor integrations, and applications of wearable flexible hybrid electronics in healthcare, energy, and environment. Adv Mater. 2020;32:1901924.
2. Shi J, Liu S, Zhang L, Yang B, Shu L, Yang Y, et al. Smart textile-integrated microelectronic systems for wearable applications. Adv Mater. 2020;32:1901958.

3. Xu C, Song Y, Han M, Zhang H. Portable and wearable self-powered systems based on emerging energy harvesting technology. Microsyst Nanoeng. 2021;7:1–14.
4. White BE Jr. Energy-harvesting devices: beyond the battery. Nat Nanotechnol. 2008;3:71–72.
5. Mathews I, Kantareddy SN, Buonassisi T, Peters IM. Technology and market perspective for indoor photovoltaic cells. Joule. 2019;3:1415–26.
6. Pecunia V, Occhipinti LG, Hoye RLZ. Emerging indoor photovoltaic technologies for sustainable internet of things. Adv Energy Mater. 2021;11:2100698.
7. Li M, Igbari F, Wang Z-K, Liao L-S. Indoor thin-film photovoltaics: progress and challenges. Adv Energy Mater. 2020;10:2000641.
8. Russ B, Glaudell A, Urban JJ, Chabinyc ML, Segalman RA. Organic thermoelectric materials for energy harvesting and temperature control. Nat Rev Mater. 2016;1:16050.
9. Yee SK, LeBlanc S, Goodson KE, Dames C. $ per W metrics for thermoelectric power generation: beyond ZT. Energy Environ Sci. 2013;6:2561–71.
10. Ryu H, Yoon H-J, Kim S-W. Hybrid energy harvesters: toward sustainable energy harvesting. Adv Mater. 2019;31:1802898.
11. Best Research-Cell Efficiencies, The National Renewable Energy Laboratory (NREL): https://www.nrel.gov/pv/cell-efficiency.html. Accessed Sep 2022.
12. Yu G, Gao J, Hummelen JC, Wudl F, Heeger AJ. Polymer photovoltaic cells: enhanced efficiencies via a network of internal donor-acceptor heterojunctions. Science 1995;270:1789–91.
13. Li G, Zhu R, Yang Y. Polymer solar cells. Nat Photonics. 2012;6:153–61.
14. Heeger AJ. 25th anniversary article: bulk heterojunction solar cells: understanding the mechanism of operation. Adv Mater. 2014;26:10–28.
15. Huang Y, Kramer EJ, Heeger AJ, Bazan GC. Bulk heterojunction solar cells: morphology and performance relationship. Chem Rev. 2014;114:7006–43.
16. Lu L, Zheng T, Wu Q, Schneider AM, Zhao D, Yu L. Recent advances in bulk heterojunction polymer solar cells. Chem Rev. 2015;115:12666–731.
17. Cui Y, Xu Y, Yao H, Bi P, Hong L, Zhang J, et al. Single-junction organic photovoltaic cell with 19% efficiency. Adv Mater. 2021;33:2102420.
18. He C, Chen Z, Wang T, Shen Z, Li Y, Zhou J, et al. Asymmetric electron acceptor enables highly luminescent organic solar cells with certified efficiency over 18%. Nat Commun. 2022;13:1–11.
19. Kim S, Jahandar M, Jeong JH, Lim DC. Recent progress in solar cell technology for low-light indoor applications. Curr Altern Energy 2019;3:3–17.
20. Ryu HS, Park SY, Lee TH, Kim JY, Woo HY. Recent progress in indoor organic photovoltaics. Nanoscale. 2020;12:5792–804.
21. Mainville M, Leclerc M. Recent progress on indoor organic photovoltaics: from molecular design to production scale. ACS Energy Lett. 2020;5:1186–97.
22. Cui Y, Hong L, Hou J. Organic photovoltaic cells for indoor applications: opportunities and challenges. ACS Appl Mater Interfaces. 2020;12:38815–28.
23. Hou X, Wang Y, Lee HKH, Datt R, Miano NU, Yan D, et al. Indoor application of emerging photovoltaics–progress, challenges and perspectives. J Mater Chem A 2020;8:21503–25.
24. Xie L, Song W, Ge J, Tang B, Zhang X, Wu T, et al. Recent progress of organic photovoltaics for indoor energy harvesting. Nano Energy. 2021;82:105770.
25. Saeed MA, Kim SH, Kim H, Liang J, Woo HY, Kim TG, et al. Indoor organic photovoltaics: optimal cell design principles with synergistic parasitic resistance and optical modulation effect. Adv Energy Mater. 2021;11:2003103.
26. Xu X, Liu W, Luo X, Chen H, Wei Q, Yuan J, et al. An overview of high-performance indoor organic photovoltaics. ChemSusChem 2021;14:3428–48.
27. Jahandar M, Kim S, Lim DC. Indoor organic photovoltaics for self-sustaining IoT devices: progress, challenges and practicalization. ChemSusChem 2021;14:3449–74.
28. Cui Y, Wang Y, Bergqvist J, Yao H, Xu Y, Gao B, et al. Wide-gap non-fullerene acceptor enabling high-performance organic photovoltaic cells for indoor applications. Nat Energy. 2019;4:768–75.
29. Ma L-K, Chen Y, Chow PCY, Zhang G, Huang J, Ma C, et al. High-efficiency indoor organic photovoltaics with a band-aligned interlayer. Joule. 2020;4:1486–500.
30. Xue J, Uchida S, Rand BP, Forrest SR. 4.2% efficient organic photovoltaic cells with low series resistances. Appl Phys Lett. 2004;84:3013–5.
31. Yoo S, Domercq B, Kippelen B. Intensity-dependent equivalent circuit parameters of organic solar cells based on pentacene and C_{60}. J Appl Phys. 2005;97:103706.
32. Rand BP, Burk DP, Forrest SR. Offset energies at organic semiconductor heterojunctions and their influence on the open-circuit voltage of thin-film solar cells. Thys Rev B. 2007;75:115327.
33. Potscavage WJ, Sharma A, Kippelen B. Critical interfaces in organic solar cells and their influence on the open-circuit voltage. Acc Chem Res. 2009;42:1758–67.
34. Elumalai NK, Uddin A. Open circuit voltage of organic solar cells: an in-depth review. Energy Environ Sci. 2016;9:391–410.
35. Arai R, Furukawa S, Sato N, Yasuda T. Organic energy-harvesting devices achieving power conversion efficiencies over 20% under ambient indoor lighting. J Mater Chem A. 2019;7:20187–92.
36. Zhou Y, Khan TM, Shim JW, Dindar A, Fuentes-Hernandez C, Kippelen B. All-plastic solar cells with a high photovoltaic dynamic range. J Mater Chem A. 2014;2:3492–7.
37. Ryu S, Ha NY, Ahn YH, Park J-Y, Lee S. Light intensity dependence of organic solar cell operation and dominance switching between Shockley–Read–Hall and bimolecular recombination losses. Sci Rep. 2021;11:16781.
38. Steim R, Ameri T, Schilinsky P, Waldauf C, Dennler G, Scharber M, et al. Organic photovoltaics for low light applications. Sol Energy Mater Sol Cells. 2011;95:3256–61.
39. Lübke D, Hartnagel P, Angona J, Kirchartz T. Comparing and quantifying indoor performance of organic solar cells. Adv Energy Mater. 2021;11:2101474.
40. Ho JKW, Yin H, So SK. From 33% to 57%—an elevated potential of efficiency limit for indoor photovoltaics. J Mater Chem A 2020;8:1717–23.
41. Shockley W, Queisser HJ. Detailed balance limit of efficiency of *p-n* junction solar cells. J Appl Phys. 1961;32:510–9.
42. Freunek M, Freunek M, Reindl LM. Maximum efficiencies of indoor photovoltaic devices. IEEE J Photovolt. 2013;3:59–64.
43. Teran AS, Wong J, Lim W, Kim G, Lee Y, Blaauw D, et al. AlGaAs photovoltaics for indoor energy harvesting in mm-scale wireless sensor nodes. IEEE Trans Electron Devices. 2015;62:2170–5.
44. Yan C, Barlow S, Wang Z, Yan H, Jen AK-Y, Mardar S, et al. Non-fullerene acceptors for organic solar cells. Nat Rev Mater. 2018;3:18003.
45. Hou J, Inganäs O, Friend RH, Gao F. Organic solar cells based on non-fullerene acceptors. Nat Mater 2018;17:119–28.
46. Zhang G, Zhao J, Chow PCY, Jiang K, Zhang J, Zhu Z, et al. Nonfullerene acceptor molecules for bulk heterojunction organic solar cells. Chem Rev. 2018;118:3447–507.
47. Armin A, Li W, Sandberg OJ, Xiao Z, Ding L, Nelson J, et al. A history and perspective of non-fullerene electron acceptors for organic solar cells. Adv Energy Mater. 2021;11:20003570.

48. Mori S, Gotanda T, Nakano Y, Saito M, Todori K, Hosoya M. Investigation of the organic solar cell characteristics for indoor LED light applications. Jpn J Appl Phys. 2015;54:071602.
49. Lee HKH, Li Z, Durrant JR, Tsoi WC. Is organic photovoltaics promising for indoor applications? Appl Phys Lett. 2016;108:253301.
50. Lechêne BP, Cowell M, Pierre A, Evans JW, Wright PK, Arias AC. Organic solar cells and fully printed super-capacitors optimized for indoor light energy harvesting. Nano Energy. 2016;26:631–40.
51. Cutting CL, Bag M, Venkataraman D. Indoor light recycling: a new home for organic photovoltaics. J Mater Chem C. 2016;4:10367–70.
52. Aoki Y. Photovoltaic performance of organic photovoltaics for indoor energy harvester. Org Electron. 2017;48:194–7.
53. Yang SS, Hsieh Z-C, Keshtov ML, Sharma GD, Chen F-C. Toward high-performance polymer photovoltaic devices for low-power indoor applications. Sol RRL. 2017;1:1700174.
54. Lee HKH, Wu J, Barbé, Jain SM, Wood S, Speller EM, et al. Organic photovoltic cells—promising indoor light harvesters for self-sustainable electronics. J Mater Chem A 2018;6:5618–26.
55. Yin H, Ho JKW, Cheung SH, Yan RJ, Chiu KL, Hao X, et al. Designing a ternary photovoltaic cell for indoor light harvesting with a power conversion efficiency exceeding 20%. J Mater Chem A. 2018;6:8579–85.
56. Goo JS, Shin S-C, You Y-J, Shim JW. Polymer surface modification to optimize inverted organic photovoltaic devices under indoor light conditions. Sol Energy Mater Sol Cells. 2018;184:31–7.
57. Yin H, Chen S, Cheung SH, Li HW, Xie Y, Tsang SW, et al. Porphyrin-based thick-film bulk-heterojunction solar cells for indoor light harvesting. J Mater Chem C. 2018;6:9111–8.
58. Goo JS, Lee J-H, Shin S-C, Park J-S, Shim JW. Undoped ZnO electrodes for low-cost indoor organic photovoltaics. J Mater Chem A. 2018;6:23464–72.
59. Shim S-C, Koh CW, Vincent P, Goo JS, Bae J-H, Lee J-J, et al. Ultra-thick semi-crystalline photoactive donor polymer for efficient indoor organic photovoltaics. Nano Energy. 2019;58:466–75.
60. Arai R, Furukawa S, Hidaka Y, Komiyama H, Yasuda T. High-performance organic energy-harvesting devices and modules for self-sustainable power generation under ambient indoor lighting environments. ACS Appl Mater Interfaces. 2019;11:9259–64.
61. You Y-J, Song CE, Hoang QV, Kang Y, Goo JS, Ko D-H, et al. Highly efficient indoor organic photovoltaics with spectrally matched fluorinated phenylene-alkoxybenzothisdiazole-based wide bandgap polymers. Adv Funct Mater. 2019;29:1901171.
62. Cui Y, Yao H, Zhang T, Hong L, Gao B, Xian K, et al. 1 cm^2 organic photovoltaic cells for indoor application with over 20% efficiency. Adv Mater. 2019;31:1904512.
63. Singh R, Chochos CL, Gregoriou VG, Nega AD, Kim M, Kumar M, et al. Highly efficient indoor organic solar cells by voltage loss minimization through fine-tuning of polymer structures. ACS Appl Mater Interfaces. 2019;11:36905–16.
64. Dayneko SV, Pahlevani M, Welch GC. Indoor photovoltaics: photoactive material selection, greener ink formulations, and slot-die coated active layers. ACS Appl Mater Interfaces. 2019;11:46017–25.
65. Nam M, Baek S, Ko D-H. Unraveling optimal interfacial conditions for highly efficient and reproducible organic photovoltaics under low light levels. Appl Surf Sci. 2020;526:146632.
66. Yin H, Ma L-K, Yan J, Zhang Z, Cheung AMH, Zhang J, et al. Thick-film low driving-force indoor light harvesters. Sol RRL. 2020;4:2000291.
67. Rodríguez-Martínez X, Riera-Galindo S, Cong J, Österberg T, Campoy-Quiles M, Inganäs O. Matching electron transport layers with a non-halogenated and low synthetic complexity polymer:fullerene blend for efficient outdoor and indoor organic photovoltaics. J Mater Chem A 2022;10:10768–79.
68. Chen C-H, Ting H-C, Li Y-Z, Lo Y-C, Sher P-H, Wang J-K, et al. New D–A–A-configured small-molecule donors for high-efficiency vacuum-processed organic photovoltaics under ambient light. ACS Appl Mater Interfaces. 2019;11:8337–49.
69. Singh R, Shin S-C, Lee H, Kim M, Shim JW, Cho K, et al. Ternary blend strategy for achieving high-efficiency organic photovoltaic devices for indoor applications. Chem Eur J 2019;25:6154–61.
70. Nam M, Noh HY, Cho J, Park Y, Shin S-C, Kim J-A, et al. All-day operating quaternary blend organic photovoltaics. Adv Funct Mater. 2019;29:1900154.
71. Nam M, Kang J, Shin J, Na J, Park Y, Cho J, et al. Ternary organic blend approaches for high photovoltaic performance in versatile applications. Adv Energy Mater. 2019;9:1901856.
72. Park S, Ahn H, Kim J, Park JB, Kim J, Im SH, et al. High-performance and stable nonfullerene acceptor-based organic solar cells for indoor to outdoor light. ACS Energy Lett. 2020;5:170–9.
73. Je H-I, Shin E-Y, Lee KJ, Ahn H, Park S, Im SH, et al. Understanding the performance of organic photovoltaics under indoor and outdoor conditions: effects of chlorination of donor polymers. ACS Appl Mater Interfaces. 2020;12:23181–9.
74. Liao CY, Chen Y, Lee C-C, Wang G, Teng N-W, Lee C-H, et al. Processing strategies for an organic photovoltaic module with over 10% efficiency. Joule. 2020;4:189–206.
75. Ding Z, Zhao R, Yu Y, Liu J. All-polymer indoor photovoltaics with high open-circuit voltage. J Mater Chem A 2019;7:26533–9.
76. Cho Y, Kumari T, Jeong S, Lee SM, Jeong M, Lee B, et al. Guest-oriented non-fullerene acceptors for ternary organic solar cells with over 16.0% and 22.7% efficiencies under one-sun and indoor light. Nano Energy. 2020;75:104896.
77. Singh R, Duan T, Kan Z, Chochos CL, Kini GP, Kumar M, et al. Revealing the structural effects of non-fullerene acceptors on the performances of ternary organic photovoltaics under indoor light conditions. Nano Energy. 2020;75:104934.
78. Liu J, Cui Y, Zu Y, An C, Xu B, Yao H, et al. Organic photovoltaic cells for low light applications offering new scope. Org Electron. 2020;85:105798.
79. Han YW, Jung CH, Lee HS, Jeon SJ, Moon DK. High-performance nonfullerene organic photovoltaics applicable for both outdoor and indoor environments through directional photon energy transfer. ACS Appl Mater Interfaces. 2020;12:3847–82.
80. Kwon NY, Park SH, Kang H, Takaloo AV, Harit AK, Woo HY, et al. Rational design of a main chain conjugated copolymer having donor–acceptor heterojunctions and its application in indoor photovoltaic cells. J Mater Chem A 2020;8:20091–100.
81. Farahat ME, Laventure A, Anderson MA, Mainville M, Tintori F, Leclerc M, et al. Slot-die-coated ternary organic photovoltaics for indoor light recycling. ACS Appl Mater Interfaces. 2020;12:43684–93.
82. Bai Y, Yu R, Bai Y, Zhou E, Hayat T, Alsaedi A, et al. Ternary blend strategy in benzotriazole-based organic photovoltaics for indoor applications. Green Energy Environ. 2021;6:920–8.
83. Wang J, Gao Y, Yu Y, Zhao R, Zhang L, Liu J. All-polymer indoor photovoltaics based on polymer acceptors with various bandgap. Org Electron. 2021;92:106134.
84. Park SH, Kwon NY, Kim HJ, Cho E, Kang H, Harit AK, et al. Nonhalogenated solvent-processed high-performance indoor photovoltaics made of new conjugated terpolymers with optimized monomer compositions. ACS Appl Mater Interfaces. 2021;13:13487–98.
85. Bai F, Zhang J, Zeng A, Zhao H, Duan K, Yu H, et al. A highly crystalline non-fullerene acceptor enabling efficient indoor organic photovoltaics with high EQE and fill factor. Joule. 2021;5:1231–45.
86. Li X, Luo S, Sun H, Sung HH-Y, Yu H, Liu T, et al. Medium band-gap non-fullerene acceptors based on a benzothiophene

donor moiety enabling high-performance indoor organic photovoltics. Energy Environ Sci. 2021;14:4555–63.
87. Chen Z, Wang T, Wen Z, Lu P, Qin W, Yin H, et al. Trap state induced recombination effects on indoor organic photovoltaic cells. ACS Energy Lett. 2021;6:3203–11.
88. Zhou X, Wu H, Lin B, Naveed HB, Xin J, Bi Z, et al. Different morphology dependence for efficient indoor organic photovoltaics: the role of the leakage current and recombination losses. ACS Appl Mater Interfaces. 2021;13:44604–14.
89. Zhang Y, Wang N, Wang Y, Zhang J, Liu J, Wang L. All-polymer indoor photovoltaic modules. iScience. 2021;24:103104.
90. Park SY, Labanti C, Luke J, Chin Y-C, Kim J-S. Organic bilayer photovoltaics for efficient indoor light harvesting. Adv Energy Mater. 2022;12:2103237.
91. Radford CL, Mudiyanselage PD, Stevens AL, Kelly TL. Heteroatoms as rotational blocking groups for non-fullerene acceptors in indoor organic solar cells. ACS Energy Lett. 2022;7:1635–41.
92. Luo S, Bai F, Zhang J, Zhao H, Angunawela I, Zou X, et al. Optimizing spectral and morphological match of nonfullerene acceptors toward efficient indoor organic photovoltaics with enhanced light source adaptability. Nano Energy. 2022;98:107281.
93. Nam M, Lee C, Ko D-H. Sequentially processed quaternary blends for high-performance indoor organic photovoltaic applications. Chem Eng J. 2022;438:135576.
94. Sun C, Pan F, Bin H, Zhang J, Xue L, Qiu B, et al. A low cost and high performance polymer donor material for polymer solar cells. Nat Commun. 2018;9:743.
95. Sun K, Xiao Z, Lu S, Zajaczkowski W, Pisula W, Hanssen E, et al. A molecular nematic liquid crystalline material for high-performance organic photovoltaics. Nat Commun. 2015;6:6013.
96. Komiyama H, To T, Furukawa S, Hidaka Y, Shin W, Ichikawa T, et al. Oligothiophene–indandione-linked narrow-band gap molecules: impact of π-conjugated chain length on photovoltaic performance. ACS Appl Mater Interfaces. 2018;10:11083–93.
97. Lin Y, Wang J, Zhang Z-G, Bai H, Li Y, Zhu D, et al. An electron acceptor challenging fullerenes for efficient polymer solar cells. Adv Mater. 2015;27:1170–4.
98. Yuan J, Zhang Y, Zhou L, Zhang G, Yip H-L, Lau T-K, et al. Single-junction organic solar cell with over 15% efficiency using fused-ring acceptor with electron-deficient core. Joule. 2019;3:1140–51.
99. Wang G, Adil MA, Zhang J, Wei Z. Large-area organic solar cells: material requirements, modular designs, and printing methods. Adv Mater. 2019;31:1805089.

Sunbin Hwang received his B.Eng. degree from Kyushu University in 2012 and earned his Ph.D. from Kyushu University in 2017 under the supervision of Prof. Chihaya Adachi. Thereafter, he moved to the Korea Institute of Science and Technology (KIST) as a researcher. In 2020, he joined the research group of Prof. Takuma Yasuda at Kyushu University as a postdoctoral research fellow. His research interests include organic electronics and device physics related to organic thermoelectrics, integrated logic circuits, and organic photovoltaics based on conducting polymers.

Takuma Yasuda is a professor at the Institute for Advanced Study, Kyushu University. He received his Ph.D. from Tokyo Institute of Technology in 2005 under the supervision of Prof. Takakazu Yamamoto. After completing postdoctoral research under Prof. Takashi Kato at the University of Tokyo, in 2018, he was appointed an assistant professor at the University of Tokyo. In 2010, he moved to Kyushu University as an associate professor in the research group of Prof. Chihaya Adachi. In 2014, he was appointed a professor at Kyushu University. His research is directed toward the design, synthesis, and functionalization of electro- and photoactive π-conjugated molecular materials, including their applications in organic photonics and electronics.